STRUCTURE AND PROPERTIES OF AN AMORPHOUS PALLADIUM-SILICON ALLOY

Thesis by

Richard Clark Crewdson

In Partial Fulfillment of the Requirements

For the Degree of

Doctor of Philosophy

California Institute of Technology

Pasadena, California

1966

(Submitted May 6, 1966)

To Helen

ACKNOWLEDGMENT

I would like to thank my advisor, Professor P. E. Duwez, who supervised my research. To work with him has been a privilege and a pleasure. D. Pope and Professor R. H. Willens each contributed valuable suggestions.

I am grateful to my wife Helen, who typed the manuscript, for her patience and encouragement during my years as a graduate student. F. G. Youngkin, L. Newkirk and M. Granoff helped with the experimental work.

Financial aid was gratefully received from the Atomic Energy Commission and from the California Institute of Technology.

ABSTRACT

A study has been made of the structure and electrical properties of an amorphous phase containing 80 at. % Pd and 20 at. % Si, obtained by rapid quenching from the liquid state. The radial distribution function, which was computed for this phase from the x-ray diffraction pattern, indicates an atomic arrangement with 11.6 nearest neighbors at an average distance of 2.79 Å. This is very similar to that of pure Pd which has twelve nearest neighbors at 2.77 Å. The diffuse diffraction pattern found by electron diffraction and the absence of detectible structure in transmission electron microscopy help to confirm the amorphous structure of the alloy. The electrical resistivity of the amorphous alloy is characterized by a very small temperature coefficient (about $9 \times 10^{-5}/^{\circ}K$ between $4^{\circ}K$ and $625^{\circ}K$). The resistivity of the liquid alloy was also measured between $1073^{\circ}K$ and $1400^{\circ}K$. A correlation was established between the resistivity of the amorphous and liquid phases. These findings are discussed on the basis of the nearly free electron theory of liquid conductors. The crystallization of the amorphous alloy was observed by transmission electron microscopy and the rate of crystallization was measured in a temperature range from 280° to $350^{\circ}C$.

TABLE OF CONTENTS

INTRODUCTION

In recent years non-crystalline metallic films have been produced by high vacuum vapor deposition (1). A few of these (such as copper-silver alloys (2)) are stable up to room temperature. Non-crystalline layers of nickel-phosphorous alloys have also been produced by electro-deposition (3).

Recently developed techniques (4,5) by which liquid alloys can be cooled at rates of the order of 10^7 °C/sec. have led to the retention of non-crystalline structures stable at room temperature. Such structures have been obtained in gold-silicon (6), gold-lead (7), and palladium-silicon (8) alloys. Amorphous structures have also been produced by this technique in tellurium-base alloys with germanium, gallium and indium (9).

Amorphous palladium-silicon alloys were chosen for this investigation because they are stable at temperatures up to 200°C. and because they can be obtained in foils large enough (about 2 cm. in diameter and 50 μ in thickness) to enable measurements of electrical and mechanical properties.

REFERENCES

1. R. Hilsch, Non Crystalline Solids, 348-373, (1960).

2. S. Mader, H. Widmer, F. M. d'Heurle, and A. S. Nowick, Applied Physics Letters, 3, 201-203, (1963).

3. J. Dixmier, K. Doi, and A. Guinier, Physics of Non Crystalline Solids, 36-48, (1965).

4. Pol Duwez and R. H. Willens, Trans. AIME (Met.), 227, 362-365, (1962).

5. P. Pietrokowsky, Rev. Sci. Instr., 34, 445-446, (1962).

6. W. Klement Jr., R. H. Willens and Pol Duwez, Nature, 187, 809, (1960).

7. P. Predecki, B. C. Giessen, N. J. Grant, Trans. AIME (Met.), 233, 1438-1439, (1965).

8. Pol Duwez, R. H. Willens and R. C. Crewdson, J. Appl. Phys., 36, 2267-2269, (1965).

9. H. L. Luo, Ph.D. Thesis, California Institute of Technology, (1964).

II. ALLOY PREPARATION AND QUENCHING TECHNIQUES

Palladium of 99.99% purity, obtained from Engelhard Industries Inc., was used with transistor grade silicon to prepare alloys in ingots of 2 to 25 g. Weighed amounts of the components were melted by induction in fused silica crucibles and under an argon atmosphere. The molten alloys did not wet the crucibles. The weight loss upon melting was small enough that in all cases the nominal composition can be taken as accurate to better than 0.1 at. %.

For x-ray and electron microscopy investigations, quenching was accomplished by use of the "gun technique"(1). In this method a small amount of the alloy ($\approx$ 25 mg.) is placed in an alumina insert of a graphite nozzle and melted by induction under an argon atmosphere. The molten metal is then propelled by a shock wave against a copper substrate. This method produces metal flakes of about one square centimeter or less in area. The flakes have the advantage that many regions are thin enough for transmission electron microscopy (2).

Foils of even cross section suitable for electrical and mechanical measurement were quenched by the "piston and anvil technique" developed by Pietrokowski (3). In this method, a molten droplet is released from a fused silica container and driven at a high speed against a copper anvil by a copper piston. The foils produced by this technique are about 2 cm. in diameter and 45 μ thick.

REFERENCES

1. Pol Duwez and R. H. Willens, Trans. AIME (Met.), 227, 362-365, (1962).

2. R. H. Willens, J. Appl. Phys., 33, 3269, (1962).

3. P. Pietrokowsky, Rev. Sci. Instr., 34, 445-446, (1962).

III. GLASS FORMATION IN PdSi ALLOYS

A. Experimental Procedure and Results. PdSi alloys, quenched by the gun technique, and with compositions between 12 at. % Si and 27 at. % Si were studied by x-ray diffraction, electron diffraction and transmission electron microscopy. X-ray diffraction patterns were obtained with a 114.6 mm.-diameter Debye Scherrer camera using MoKα radiation monochromatized by the (200) reflection of a lithium fluoride crystal. The x-ray diffraction patterns of alloys in the range of composition from 15 at. % Si to 23 at. % Si (see Fig. 3.1) exhibited only the broad diffuse rings characteristic of an amorphous, or liquid like structure. The x-ray diffraction patterns from quenched alloys outside of this range always contained sharp Bragg reflections indicating the presence of a crystalline phase as well. That the quenched alloy is amorphous between 15 at. % and 23 at. % Si is corroborated by evidence from electron diffraction and microscopy. A typical electron micrograph and electron diffraction pattern of the alloy $Pd_{80}Si_{20}$ is shown in Fig. 3.2. The lack of any sharp Bragg-type diffraction maxima, in spite of the very short wavelength of the electrons (0.037 Å), indicates the absence of crystals with grain sizes of more than about 30 Å. The Bragg reflections from crystals smaller than this would be broadened to such an extent as to exhibit a pattern

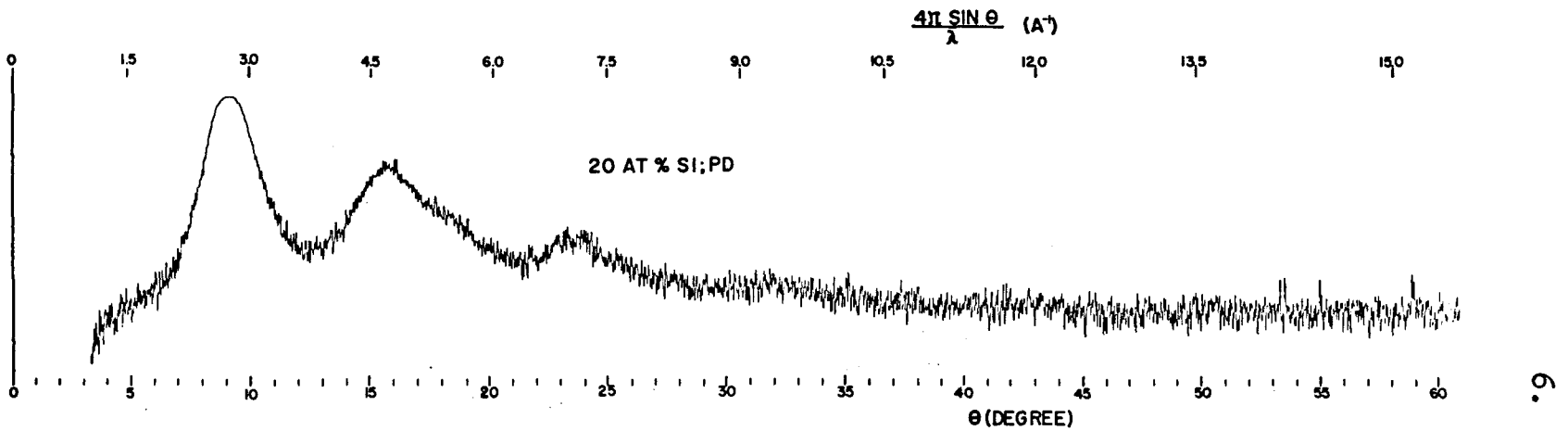

Fig. 3.1. Microphotometric trace of an x-ray diffraction pattern for the alloy Pd_{80} Si_{20}.

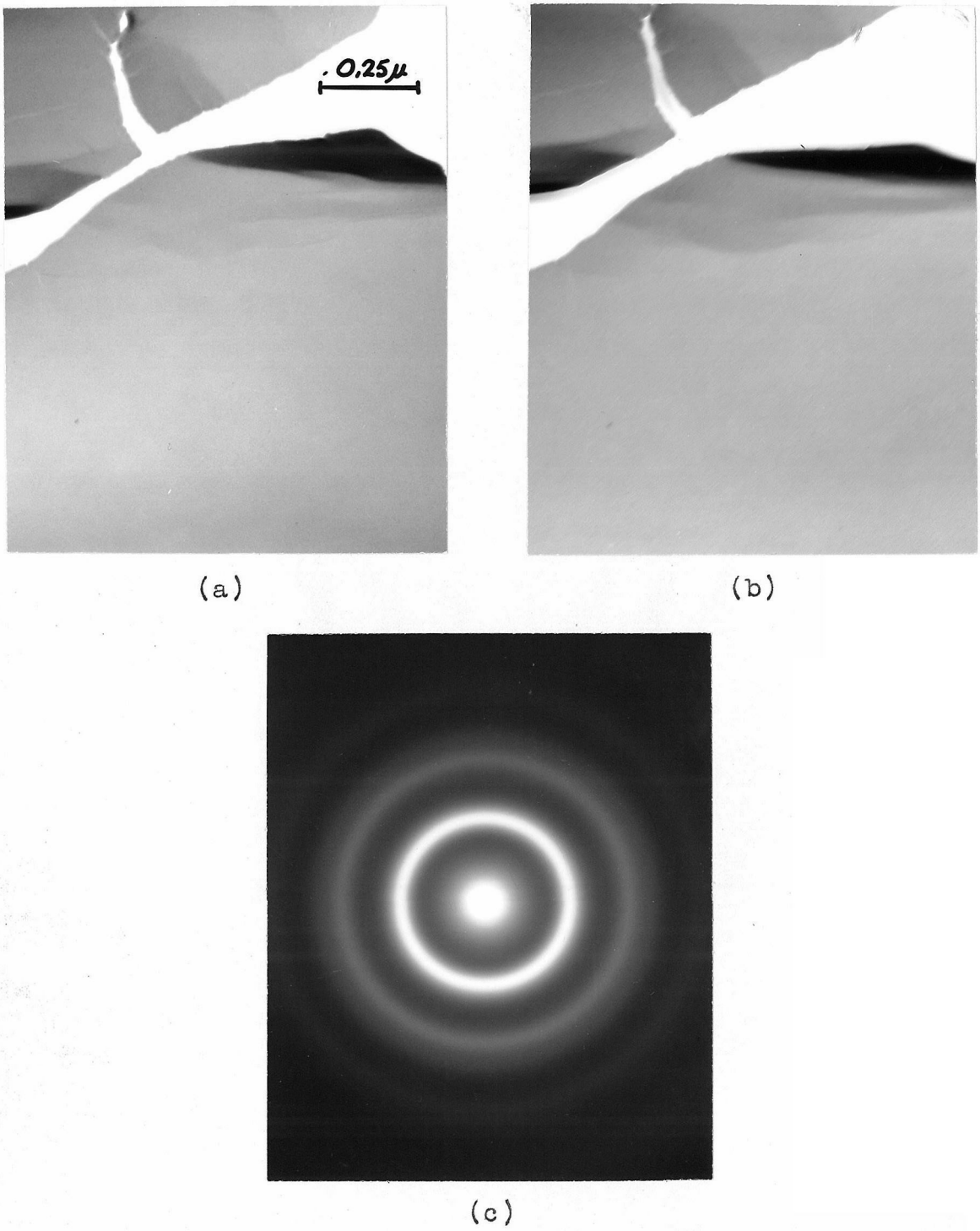

Fig. 3.2. (a) Transmission electron micrograph of a quenched $Pd_{80}Si_{20}$ alloy. (b) Same region as in (a) rotated by about 15°. (c) Electron diffraction pattern of an amorphous region. (100 kv)

indistinguishable from that of an amorphous structure. Since the regions examined by microscopy were thinner than the bulk of the quenched foil, and hence more rapidly quenched, these observations do not rule out the possibility that larger crystals exist in thicker regions of the foil.

In high magnification electron microscopy (Fig. 3.3a) and in dark field electron microscopy (Fig. 3.3b) some granularity in the image is often detected. The effect may be similar to the "micelles" (1) often found in the electron microscopy of silicate glasses and in the absence of a crystalline diffraction pattern it cannot be concluded that they are due to crystals in the substance.

Quenched foils in the composition range from 23 at. % Si to 26 at. % Si usually appeared to be amorphous when examined by transmission electron microscopy even though x-ray diffraction indicated that they were mostly crystalline. This is not surprising because the regions examined by electron microscopy are thinner than the bulk of the foil and hence more rapidly cooled. In the alloys with an Si concentration of less than 15% fcc microcrystals were observed in an amorphous matrix.

An example of microcrystals in a quenched $Pd_{86}Si_{14}$ alloy is shown in the bright field electron micrograph of Fig. 3.4a. The selected area diffraction pattern of a part of the dark "band" of strongly diffracting microcrystals seen on the right side of Fig. 3.4a is shown in

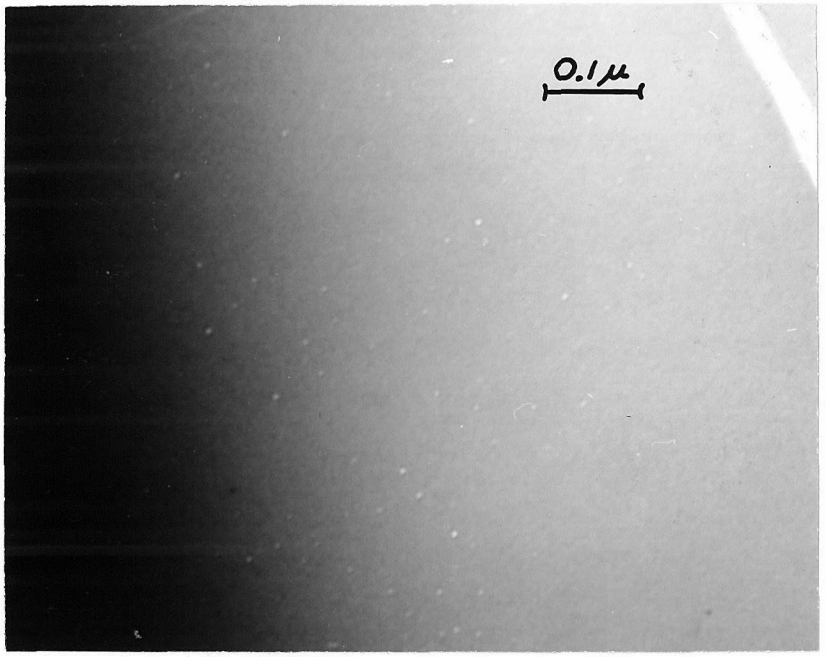

(a)

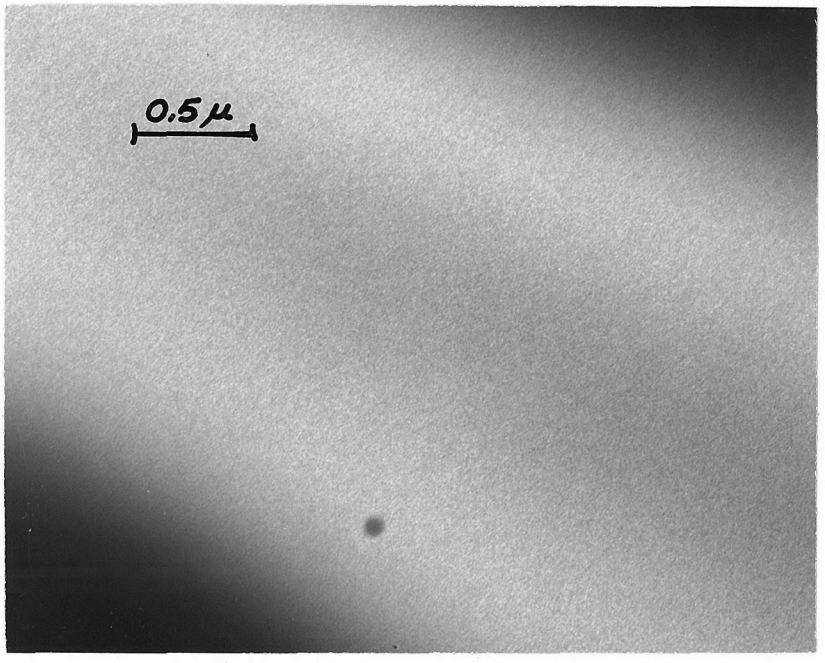

(b)

Fig. 3.3. (a) High magnification electron micrograph of a quenched $Pd_{80}Si_{20}$ alloy. (b) Dark field electron micrograph of a quenched $Pd_{80}Si_{20}$ alloy, obtained by displacing the 10 diameter objective aperture to a part of the intense low angle diffraction halo.

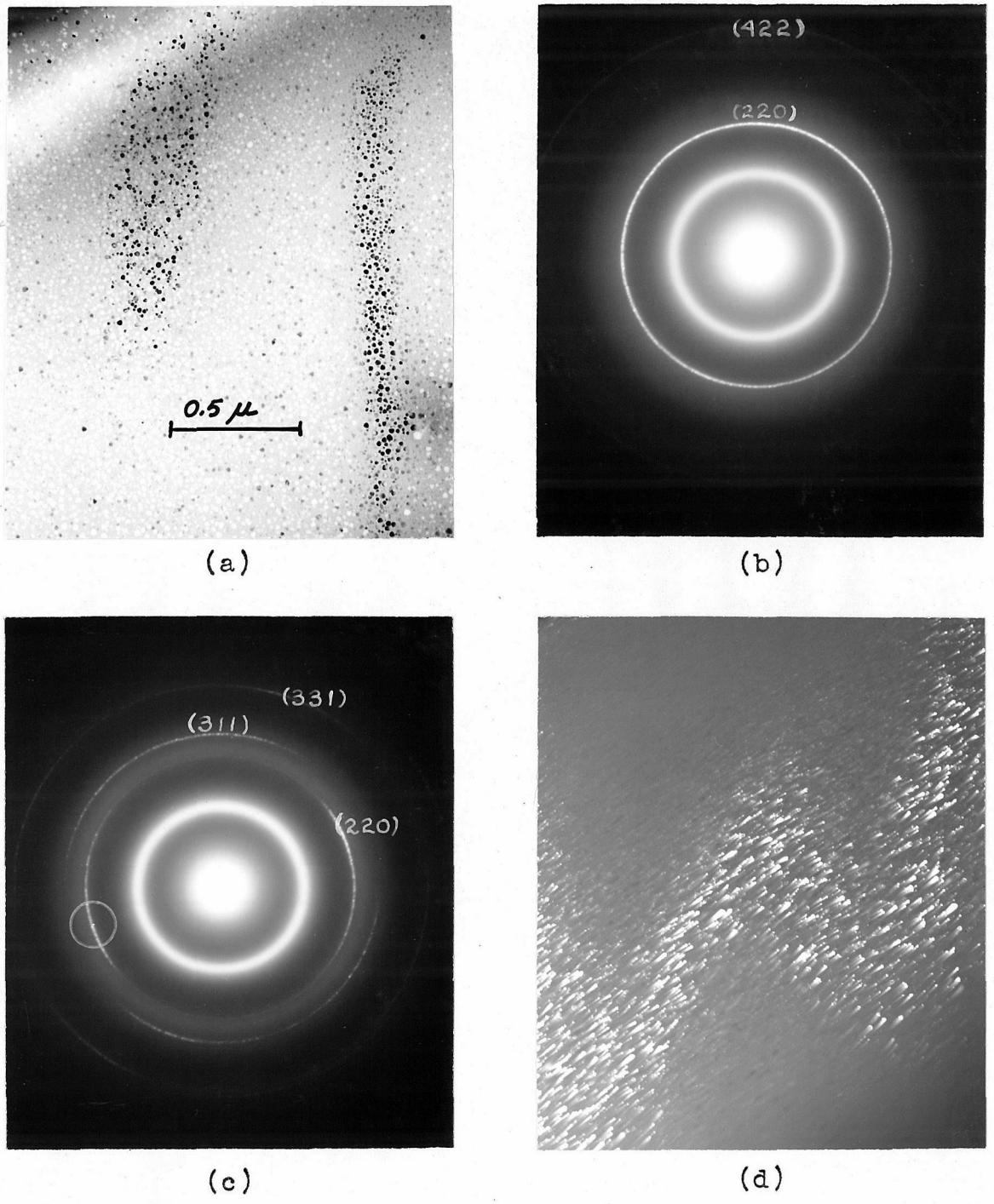

Fig. 3.4. Electron micrographs and diffraction patterns from rapid quenched $Pd_{86}Si_{14}$ alloy (100 kV). (a) Bright field micrograph showing bend contours composed of dark strongly diffracting microcrystals. (b) Selected area diffraction pattern from bend contour on right side of (a). (c) Selected area diffraction pattern from region of (a) off a bend contour. (d) Dark field micrograph made by displacing objective aperture to the circle in (c).

Fig. 3.4b. The Miller indices shown on the diffraction rings of Fig. 3.4b have been assigned on the assumption that the microcrystals are fcc. This assumption has been verified by observations of many foils. The appearance of only the (220) and (422) reflections in Fig. 3.4b indicates that the micro-crystals are oriented with their [111] direction parallel to the electron beam and the fact that these microcrystals are oriented at random about the [111] axis is implied by the almost uniform intensity around the diffraction rings. In the selected area diffraction pattern (Fig. 3.4c), of an area off the dark bands in Fig. 3.4a, the appearance of the (311) and (331) reflections, in addition to the (220) and (422), indicates that the [111] direction is tilted slightly away from the beam direction. In this case only those microcrystals in which the tilt angle is in the (220) plane remain in strongly diffracting positions, a fact that causes most of the crystals just off the dark band to appear white. Thus, the dark bands in Fig. 3.4a, which changed position when the foil was tilted, correspond to the "bend contours" in an electron micrograph of a single crystal. The fact that almost 100% of the crystals in the band on the right side of Fig. 3.4a are in strongly diffracting positions implies that their orientations with respect to the foil differ by no more than a few degrees. The bend contours are usually more prominent in dark field microscopy. A dark field micrograph obtained

of an area near to that of Fig. 3.4a is shown in Fig. 3.4d.

Face centered cubic crystals in the quenched $Pd_{80}Si_{20}$ foils, whose presence is indicated by devitrification studies (see Chapter IV), might be expected to have a [111] orientation. Although in this case the crystals are too small to be observed directly, a bend contour effect might be apparent. In a few cases (such as in Figs. 3.2a and 3.2b) changes in contrast which might be due to this effect have been observed when a specimen was rotated.

The relationship of the crystal orientation to the plane of the foil is uncertain but it is likely that the [111] is a preferred growth direction and that it is in the direction of the heat flow. In this case the [111] would be perpendicular to the foil plane. The fact that the crystals are randomly oriented about the [111] indicates that they were not epitaxially nucleated on the copper substrate.

An electron micrograph and the corresponding diffraction pattern of a $Pd_{88}Si_{12}$ alloy are shown in Fig. 3.5. The fcc crystals are larger in this alloy. Even though almost half of the foil is covered with microcrystals, it is significant that so few of them touch each other. This repulsion may be a consequence of solute rejection by Pd rich microcrystals. An attempt was made to see if there was significant solid solution in the fcc phase by measuring its lattice parameter from Debye - Scherrer x-ray films of quenched $Pd_{88}Si_{12}$ and $Pd_{97}Si_3$ alloys, and

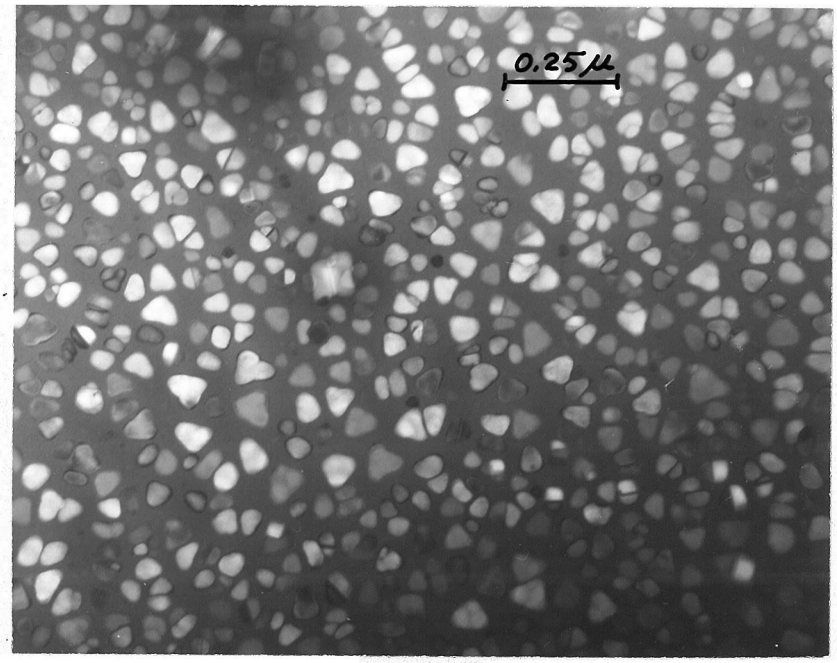

(a)

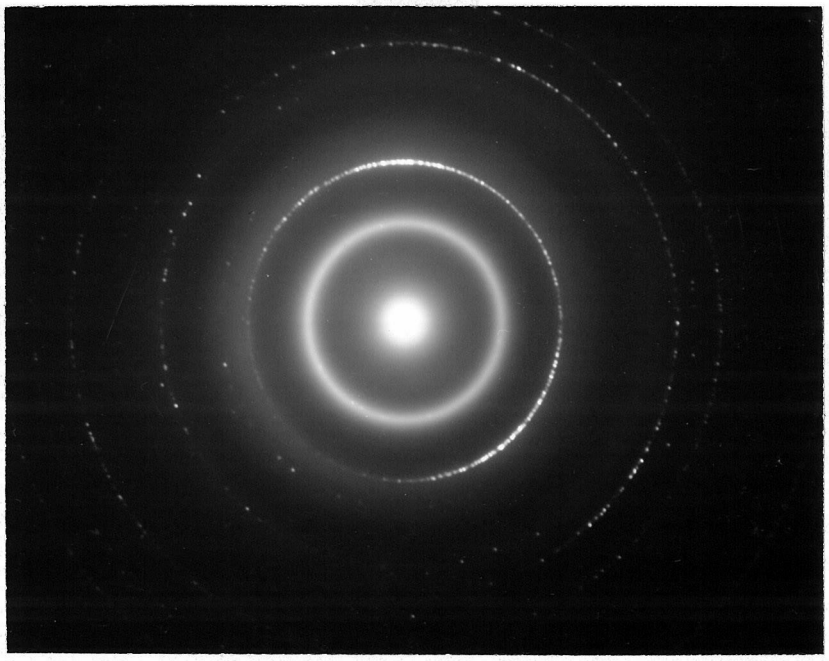

(b)

Fig. 3.5. Transmission electron micrograph and diffraction pattern from a rapid quenched Pd_{88} Si_{12} alloy. (100 kV.)

it was found that the lattice parameter was the same as that for pure Pd within the 0.001 Å experimental error. However, since the Pauling atomic radii of Si and Pd for coordination 12 are equal to within 1%, this result cannot be taken as conclusive evidence that there is no solid solution.

B. Discussion. Once a liquid has been cooled below the melting point, T_m, it is in a metastable equilibrium and crystallization takes place by a two step process of nucleation and growth. If the nucleation is homogeneous, most metal liquids can be readily cooled to a temperature λT_m °K (where $\lambda \approx 0.8$) before the nucleation frequency is significant (2).

Since the atomic configuration of a liquid is temperature dependent, it continually changes as the liquid is cooled. If crystallization can be prevented a temperature T_g is eventually reached at which the relaxation time for the undercooled liquid to attain the metastable equilibrium configuration is too long for it to be attained (3). The temperature T_g, which varies inversely with the cooling rate, is known as the glass point and below T_g the undercooled liquid is referred to as a glass. Experimentally, T_g can be determined from measurements of physical properties such as volume or heat content. When these properties are plotted against temperature it is found that their graphs

show a sharp change of slope at the glass point (Fig. 3.6). The slope is higher at temperatures above T_g, which indicates that the thermal expansion coefficient or heat capacity is higher for the liquid than for the glass. This is due to the fact that the liquid has a "configurational" degree of freedom which is lacking in the glass (3). Since it is often found that the viscosity of the liquid at the glass point is about $10^{13.6}$ poises, a glass is sometimes defined as an undercooled liquid in which the viscosity is greater than this value.

The problem of producing a glass in an alloy thus reduces to one of attaining a cooling rate fast enough to suppress crystallization in the "critical temperature range" between λT_m and T_g. This will occur if the rate is fast enough to suppress the nucleation to a temperature below which the growth velocity is no longer fast enough to prevent crystallization. It is apparent that the smaller the quantity $(\lambda T_m - T_g)$ for a given alloy, the easier it is to form a glass in that alloy. In fact, it has been shown by Turnbull and Cohen (4) that the crystallization tendency of different systems varies with the quantity $\left(\lambda \frac{kT_m}{h_v} - \frac{kT_g}{h_v}\right)$ where k is the Boltzman constant and h_v is the heat of vaporization.

By using the above concepts it is possible to give a

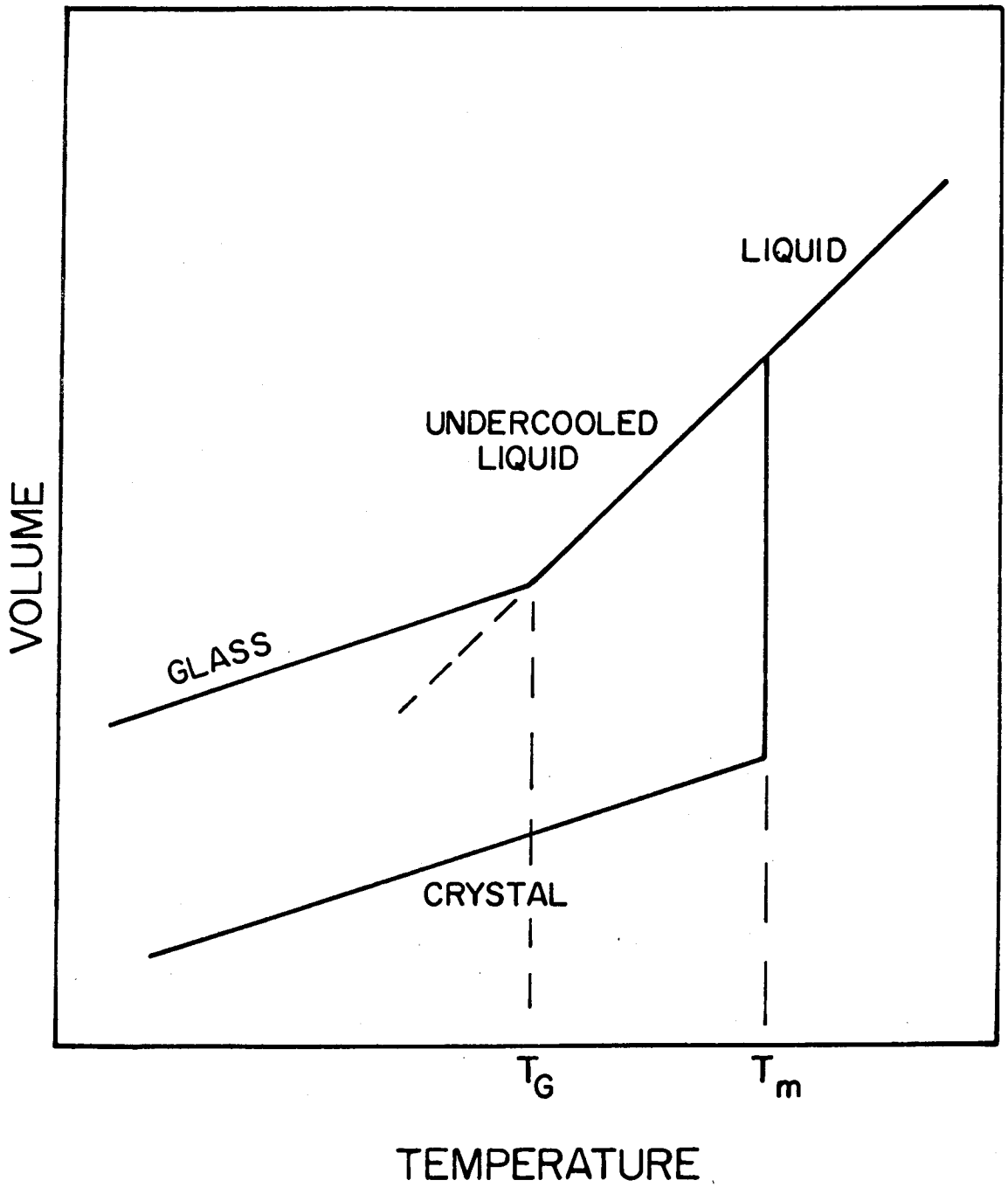

Fig. 3.6. Temperature dependence of the volume of different phases in an ideal glass forming system.

qualitative explanation for the occurrence of the amorphous phase in PdSi alloys. According to the PdSi phase diagram (5) shown in Fig. 3.7 the glass forming compositions lie in the vicinity of a low temperature (about 800°C) eutectic at about 15 at. % Si. This fact is significant since it means that T_m is very low with respect to pure Pd. The steepness of the liquidus on the Pd rich side of the diagram is also significant because it means that the large difference in T_m is accompanied by a relatively small difference in composition dependent properties such as viscosity. Since the viscosity decreases rapidly with temperature this implies that the crystallization growth velocity, which varies inversely with viscosity, will be much slower than that for an equivalent degree of undercooling in pure Pd. In other words the crystallization in the eutectic alloy should be relatively sluggish.

Hilsch (7) has shown that T_g is very low for pure metals (about 20°K). However, for alloys which tend to crystallize into two phases there is a "complexity factor" introduced which tends to increase T_g because of the increase in the atomic diffusion distance necessary for crystallization. It has been shown that for the extremely high cooling rates used here, elements which are normally

---

* Recent work (6) has indicated the presence of a silicide in the vicinity of 16 at. % Si.

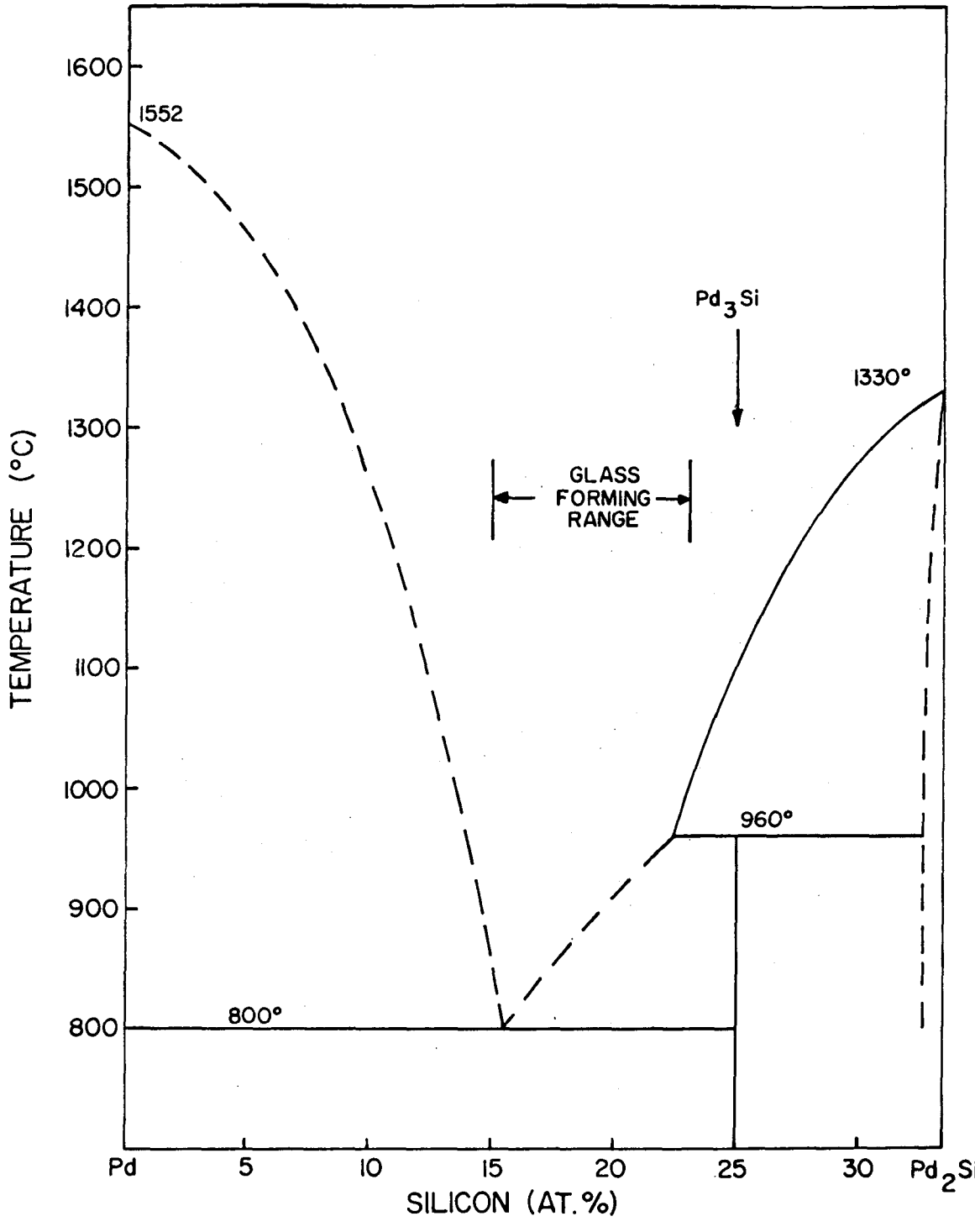

Fig. 3.7. Palladium rich side of the equilibrium phase diagram of the palladium silicon system.

insoluble are capable of crystallizing as a solid solution. Thus, the effectiveness of this complexity factor in increasing T_g will depend to some extent upon the incompatibility of the metals involved. This might, for example, be expressed by Hume-Rothery's rules, or measured by the extent of solid solution at equilibrium. In the case of PdSi it is not known a priori just how effective the complexity factor is, but the different electronegativity of Si and Pd suggest that it might be considerable.

An additional factor peculiar to the PdSi alloys which is also conducive to glass formation is that the molten alloys in the vicinity of the eutectic readily undercool in bulk by as much as 125°C (8) without any precautions being taken. This implies that heterogeneous nucleation is not very effective in PdSi alloys. By studying the undercooling of small droplets, Duwez (9) has shown that homogeneous nucleation does not become significant until about 575°C ($\lambda \approx 0.78$). Since, as will be shown in Chapter VI, the glass point, T_g, for the alloy $Pd_{80}Si_{20}$ is approximately 430°C, the critical temperature difference ($\lambda T_m - T_g$) is only about 145°C in $Pd_{80}Si_{20}$. This compares with a difference of about 1500°C expected for pure Pd.

The relatively sharp demarcation, on rapid quenching, between the amorphous and crystalline forming regions at

15 at. % Si is not clearly understood. It may be that the fcc crystals observed by electron microscopy, in alloys with less than the eutectic concentration of Si, are primary Pd. The presence of the silicide near 16 at. % Si may also be significant since fcc Pd is an equilibrium phase only at Si concentrations of less than that of the silicide.

The most important point in the above discussion is that in any system, glass formation is particularly likely in the vicinity of a low temperature eutectic. Thus, by analogy to the results obtained above it might be expected that similar alloy systems such as PtSi, PtSb, PtGe, and RhGe which all exhibit relatively low temperature eutectics on the platinum metal side of the phase diagram would also form glasses on rapid quenching. It has been found that in regions of quenched foils suitable for transmission electron microscopy, glass is actually formed in these systems for alloys near the eutectic composition (10).

REFERENCES

1. J. Zarzycki and R. Mezard, Compt. Rend., 254, 1755-1757, (1962).
2. D. Turnbull, J. Chem. Phys., 18, 769, (1950).
3. G. O. Jones, Glass, (1956).
4. D. Turnbull and M. H. Cohen, Mod. Aspects of the Vitrious State, I, 38-62, (1960).
5. M. Hanson and K. Anderko, Constitution of Binary Alloys, 1125-1126, (1958).
6. P. Duwez, Private Communication.
7. R. Hilsch, Non Crystalline Solids, 348-373, (1960).
8. P. Lebeau and P. Jolibois, Compt. Rend., 146, 1028-1031, (1908).
9. P. Duwez, Private Communication.
10. R. C. Crewdson and P. Duwez, to be published.

IV. THE RADIAL DISTRIBUTION FUNCTION OF AMORPHOUS $Pd_{80}Si_{20}$

A. Experimental Procedure. The well known method (1) of applying the Fourier integral theorem to x-ray diffraction data was used to calculate the radial distribution function of $Pd_{80}Si_{20}$. X-ray diffraction photographs were made using a 114.6 mm. diameter Debye-Scherrer camera with molybdenum $K\alpha$ radiation monochromatized by the (200) plane of a lithium fluoride crystal. To provide for later determination of the background density, small regions at both ends of the film were shielded by lead. The specimen consisted of +200 mesh flakes of $Pd_{80}Si_{20}$ quenched by the gun method and packed in a glass capillary. Two exposures, of 95 hours and 30 hours respectively, were made of the specimen at 45 kv and 18 ma. An additional 95 hour exposure was made of the unfilled glass capillary.

A calibration film was made by exposing small sections of a film to the monochromatized x-ray beam for varying lengths of time. With the use of this film it was possible to relate the film density to the intensity (in arbitrary units) of the incident x-ray beam.

To make certain that development conditions were constant, the 95 hour exposures of the $Pd_{80}Si_{20}$ and capillary specimens, along with a calibration film, were developed simultaneously and with constant agitation of the developing solution. The 30 hour exposure of the $Pd_{80}Si_{20}$ was developed separately along with its own calibration film.

It was necessary to know how densely the flakes of $Pd_{80}Si_{20}$ were packed into the capillary in order to make a correction for absorption of the x-ray beam by the specimen. The average "packing density" was determined from the weight of the flakes packed into the capillary and the dimensions of the cylindrical volume into which they were packed. The packing density of the specimen used here, expressed as a percentage of the density of the amorphous $Pd_{80}Si_{20}$ (see Appendix B) was 20.9% $\pm$ 1%. Two other specimens, treated in a similar way, had packing densities of 20.7% and 18.8%. The low density is a consequence of the acicular shape of the flakes.

An A.R.L. microphotometer was used to obtain traces from the films. Distance along the trace was related to the Bragg angle, θ, through the microphotometer response to scratches which were placed a known distance apart on the film before development and the film density D was calculated from the amplitude Y of the microphotometer trace using the relation

$$D = \log\left(\frac{Y_o}{Y}\right)$$

where Y_o = amplitude of the microphotometer response to the background region. An average density was computed by averaging the results for D at corresponding angles on either side of the direct beam. The intensity, I, of the diffracted beam was calculated in arbitrary units by interpolating in a table of I vs. D obtained from the appropriate calibration film. A typical plot of I vs. D is shown in Fig. 4.1. All

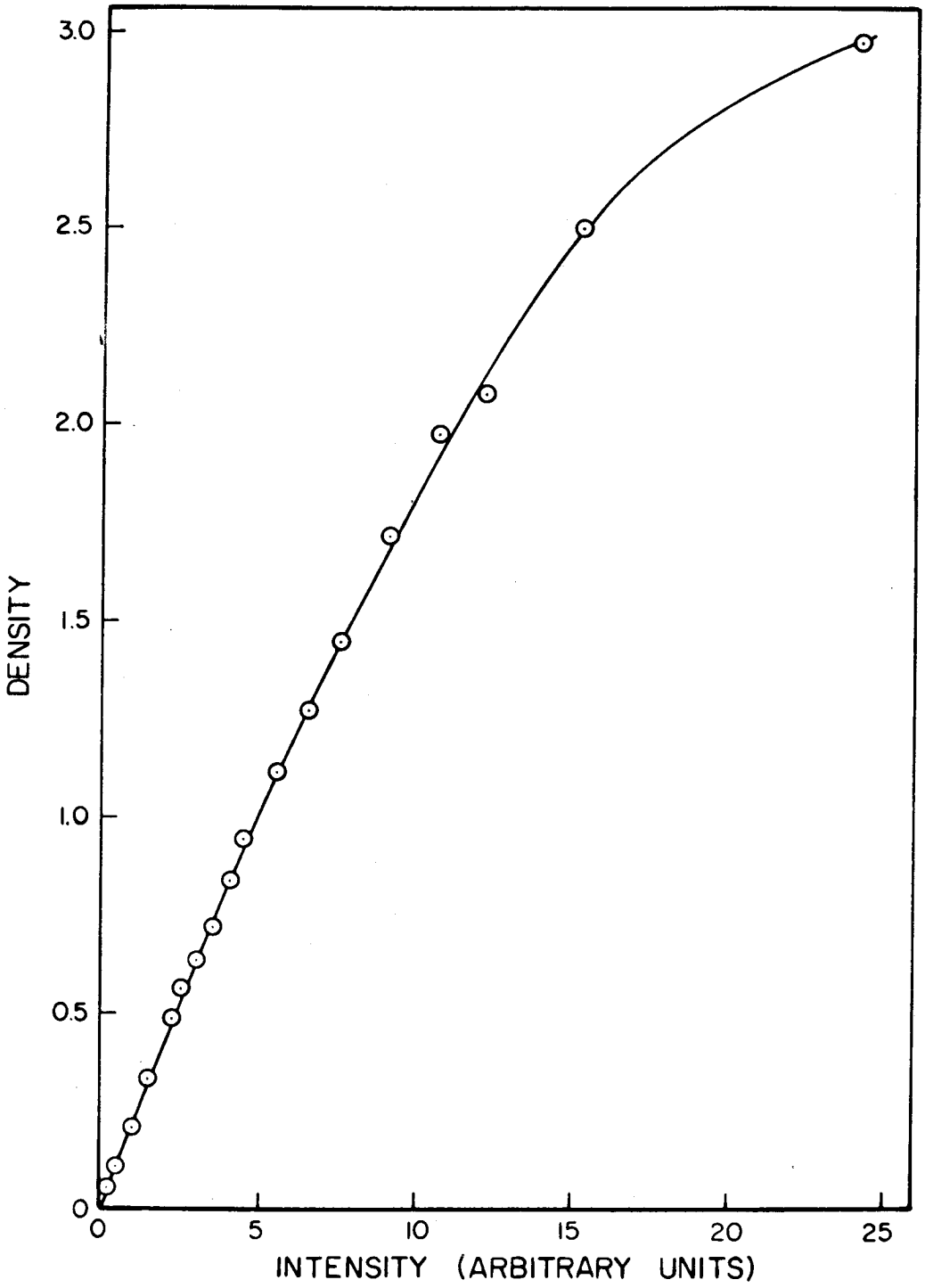

Fig. 4.1. Dependence of the density of Ansco Superay-C x-ray film upon the intensity of the MoKα x-radiation to which it was exposed.

density data taken from the 95 hour $Pd_{80}Si_{20}$ exposure, except for data in the vicinity of the intense low angle peak, fell in the region of the curve below D = 1.0. Reliable intensity data in the vicinity of the first peak was obtained from the 30 hour exposure. The matching, at the first peak, of intensity data taken from both films is shown in Fig. 4.2 where $s = \frac{4\pi \sin\theta}{\lambda}$, and λ is the x-ray wavelength.

By the above procedure the intensities $I^E_{sc,sc}$ and $I^E_{c,c}$ were obtained where:

$I^E_{sc,sc}$ = observed diffracted intensity of sample and capillary with absorption taking place in sample and capillary.

$I^E_{c,c}$ = observed diffracted intensity of capillary with absorption in capillary alone.

$I^E_{sc,sc}$ is a combination of coherently and incoherently scattered contributions from the sample and the glass capillary. In addition it is modified by polarization in the monochrometer crystal and specimen and by absorption of the diffracted x-rays in the specimen. The proper polarization factor is:

$$P(\theta) = \frac{1 + \cos^2(2\theta') \cdot \cos^2(2\theta)}{1 + \cos 2\theta'}$$

where θ' is the Bragg angle for the reflecting planes of the

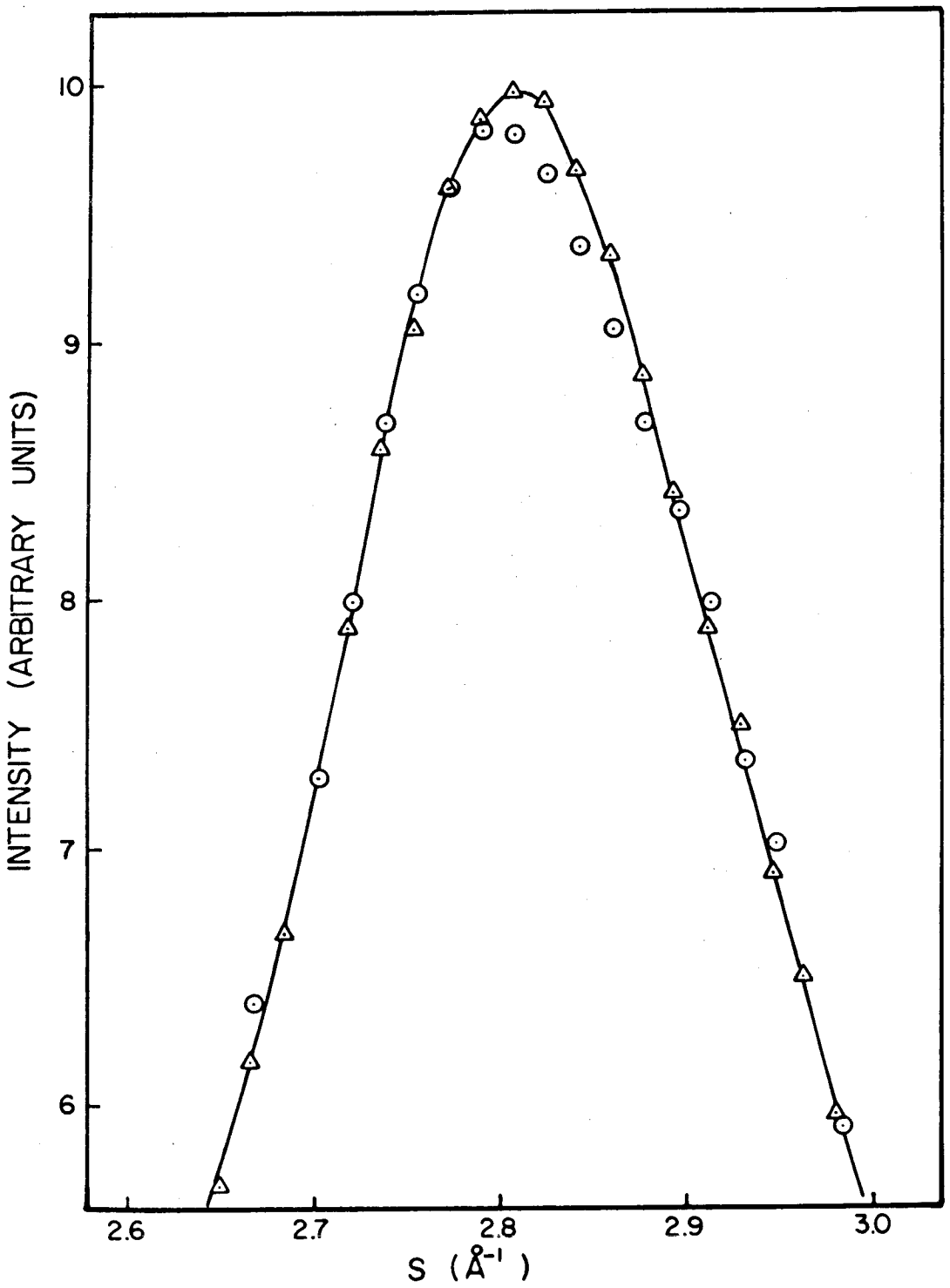

Fig. 4.2. Comparison of the diffracted x-ray intensity in the vicinity of the first diffraction peak of amorphous $Pd_{80}Si_{20}$ as determined from x-ray films with a 95 hour exposure ⊙ and a 30 hour exposure △ . The x-ray tube was operated at 35 kv and 18 ma during both exposures.

monochromatizing crystal. For the (200) planes of lithium fluoride (d=2.0135 Å) and molybdenum Kα radiation (λ = 0.71069 Å); θ' = 10.165°.

The intensity, corrected for absorption, polarization and the contribution of the capillary, was then calculated using the formula:

$$(I(s)+I_{inc})^{E} = \frac{1}{P(s)\ A_{s,sc}} \left\{ I^{E}_{sc,sc} - \frac{A_{c,sc}}{A_{c,c}} I^{E}_{c,c} \right\}$$

where $I(s)$ = intensity of coherently diffracted radiation from $Pd_{80}Si_{20}$,

I_{inc} = intensity of incoherently diffracted radiation from $Pd_{80}Si_{20}$,

$A_{s,sc}$ = sample absorption factor for absorption in sample and capillary,

$A_{c,sc}$ = capillary absorption factor for absorption in sample and capillary,

$A_{c,c}$ = capillary absorption factor for absorption in capillary only,

and the superscript E refers to experimentally determined quantities. The small magnitude of the capillary correction is shown in Fig. 4.3.

Knowledge of the linear absorption coefficients μ_s and μ_c of the powder sample and the capillary glass respectively was necessary in order to calculate the absorption factors. The coefficient μ_c was determined by measuring the attenuation of molybdenum Kα radiation in a piece of capillary glass and μ_s was computed using the formula:

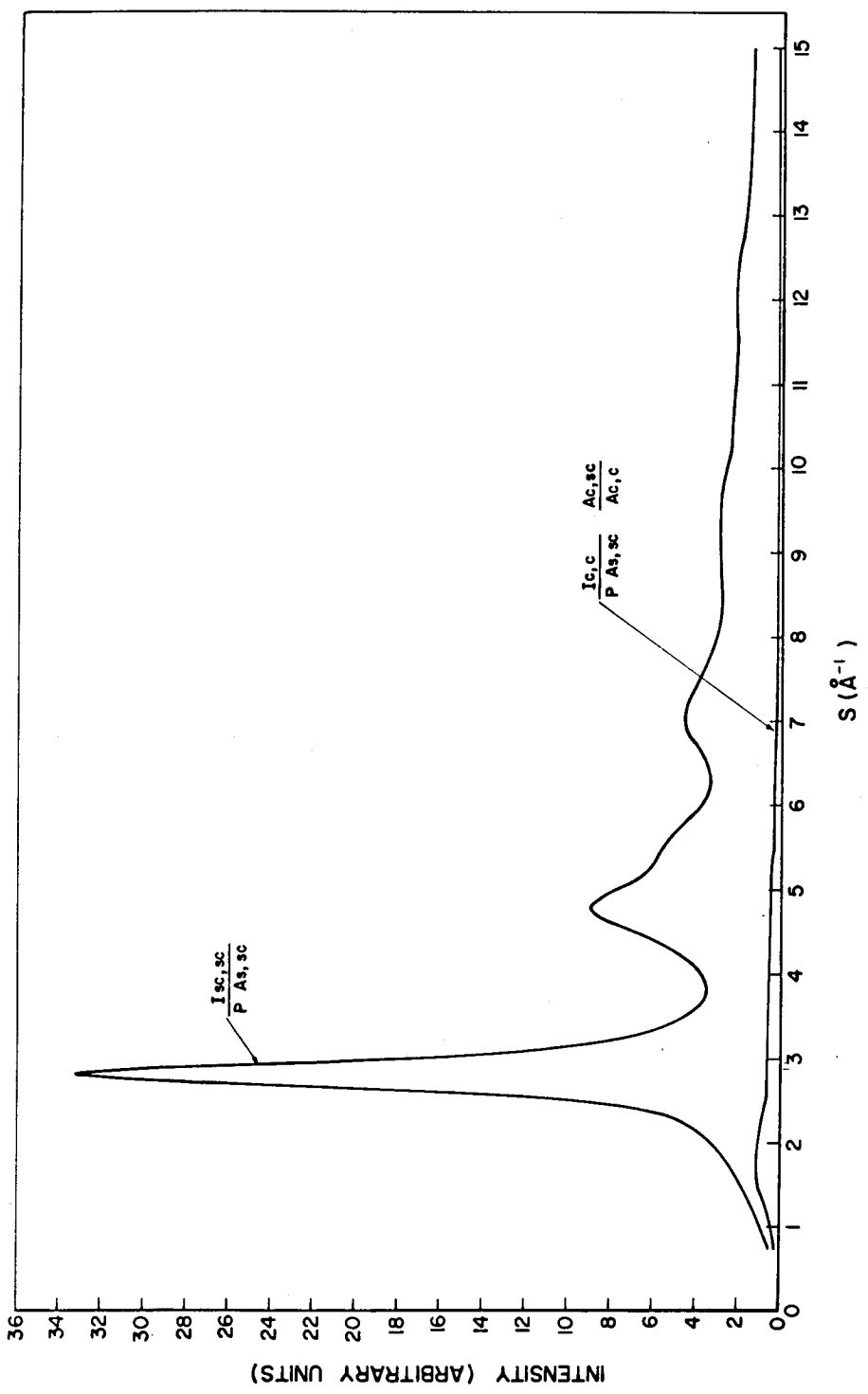

Fig. 4.3. Contributions to experimentally observed x-ray intensities diffracted from the $Pd_{80}Si_{20}$ specimen and from the capillary container.

$$\mu_s = \left\{ \sum_i m_i \left(\frac{\mu}{\rho}\right)_i \right\} \rho_s$$

where m_i is the mass fraction of the i^{th} element, $\left(\frac{\mu}{\rho}\right)_i$ is the mass absorption coefficient of the i^{th} element and ρ_s is the packing density of the packed $Pd_{80}Si_{20}$ flakes in g/cc. A program written by Pings, et al (2), for the IBM 7090 computer was used to compute the absorption coefficients.

The incoherent intensity, I_{inc}, was calculated in electron units using the formula (3):

$$I_{inc} = BZH$$

where $B = \left\{ 1 + \frac{2h\lambda}{mc} \left(\frac{\sin\theta}{\lambda}\right)^2 \right\}^{-3}$, h is Planck's constant, m the electron rest mass, c the speed of light and Z the atomic number. The function H has been given numerically by Bewilogua (4) for $Z > 6$.

The experimental intensity $(I(s) + I_{inc})^E$ must be expressed in electron units in order to carry the analysis further. The normalization uses the fact that at high Bragg angles the atoms scatter independently. The intensity in electron units of x-rays scattered from a single atom is f^2 where f equals the atomic scattering factor. A normalization factor α can then be calculated from the relation:

$$\alpha = \lim_{s \to \infty} \alpha'(s) \equiv \lim_{s \to \infty} \frac{\langle f^2 \rangle + \langle I_{inc} \rangle}{(I + I_{inc})^E}$$

where the notation $\langle \xi \rangle$ has been used to indicate the average of the quantity ξ ever all atoms. That is:

$$\langle \xi \rangle \equiv \frac{1}{N} \sum_{\substack{\text{SUM OVER} \\ \text{ALL ATOMS}}} \xi$$

where N is the total number of atoms. A difficulty of this method is the slow convergence of $\alpha'(s)$ at experimentally accessible Bragg angles. Krogh-Moe (5) has proposed a second method of calculating α which converges more quickly. That is:

$$\alpha = \lim_{s \to \infty} \alpha^{(2)}(s) \equiv \lim_{s \to \infty} \frac{\int_0^s s'^2 \left\{ \langle f^2 \rangle + \langle I_{inc} \rangle \right\} ds' - 2\pi^2 \frac{N}{V} \langle Z \rangle^2}{\int_0^s s'^2 (I + I_{inc})^E \, ds'}$$

In both cases the function $\alpha(s)$ should exhibit decreasing oscillations about a constant value α as $s \to \infty$. The magnitude of $\alpha'(s)$ and $\alpha^{(2)}(s)$ calculated for different values of s is given below.

Table 4.1

Normalization Factors Calculated for Different Upper Limits in s.

S	$\alpha'(s)$	$\alpha^{(2)}(s)$
13.0	107.4	110.3
13.5	108.9	110.2
14.0	109.4	110.2
14.5	112.5	110.2
15.0	108.2	110.3

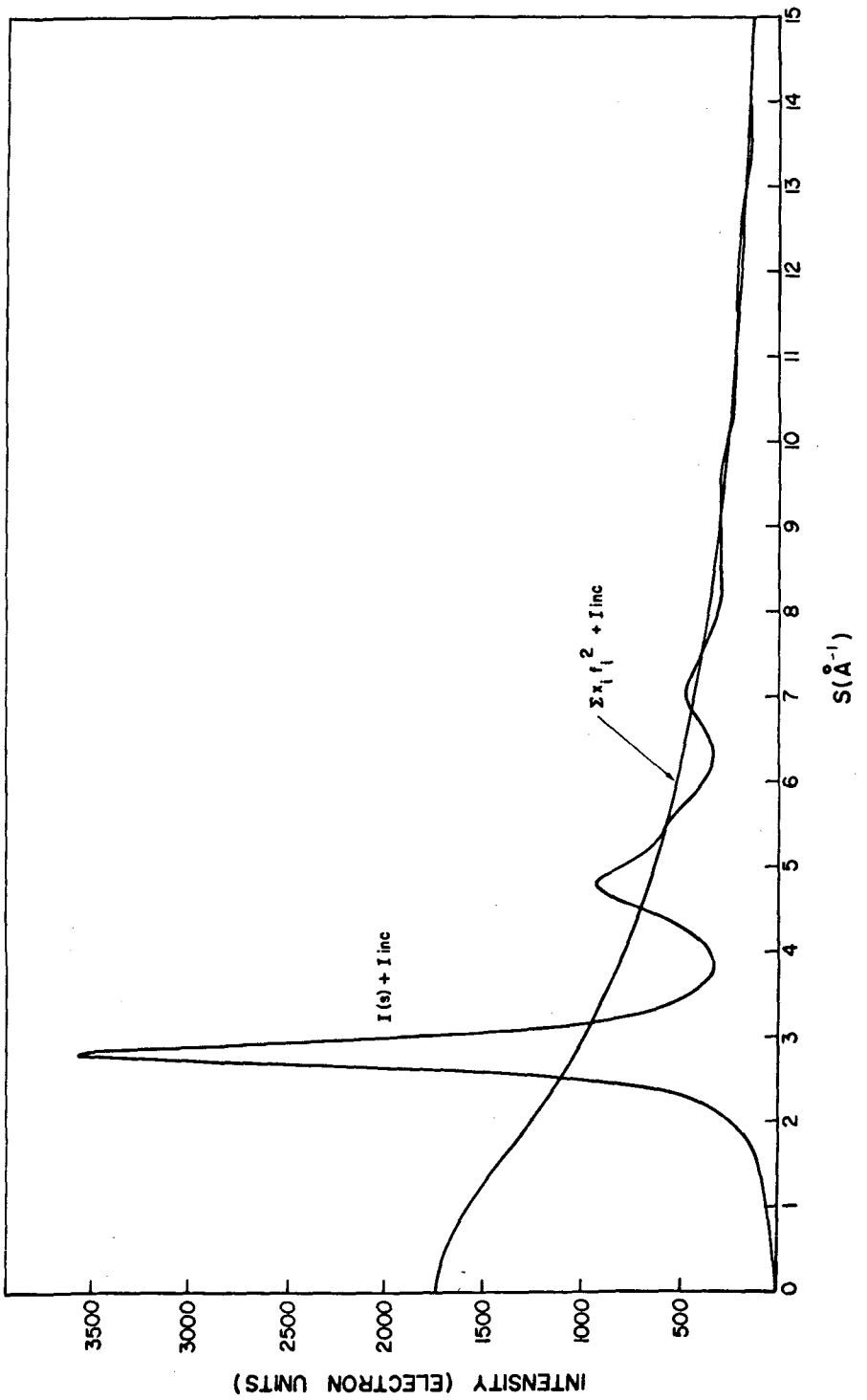

Fig. 4.4. Diffracted x-ray intensity from the amorphous $Pd_{80}Si_{20}$ alloy, corrected for absorption, polarization and diffraction from the capillary container.

The important fact that there is no steady drift in $\alpha(s)$ in addition to the oscillations is a good indication that the corrections applied to the experimental intensity have been valid. The corrected experimental intensity $(I(s) + I_{inc})^E$, expressed in electron units, is plotted in Fig. 4.4.

B. Calculation of the Radial Distribution Function

The amplitude of x-rays scattered from an array of atoms is:

$$F = \sum_{\substack{\text{SUM OVER} \\ \text{ALL ATOMS}}} f_k e^{i \vec{s} \cdot \vec{u}_k}$$

where $\vec{u}_k$ is the position vector of the k^{th} atom and $\vec{s}$ is the difference in the wave vectors of the scattered and incident radiation. Notice that:

$$s = |\vec{s}| = \frac{4\pi \sin\theta}{\lambda}$$

By squaring the scattered amplitude the total scattered intensity F^2 is obtained where:

$$F^2 = \sum_j f_j^2 + \sum_{j \neq k} f_j f_k^* e^{i \vec{s} \cdot (\vec{u}_j - \vec{u}_k)}$$

By changing to a sum over atom species and dividing through by the total number of atoms N, one obtains I(s), the scattered x-ray intensity per atom:

$$I(s) = \langle f^2 \rangle + \sum_{ij} f_i f_j \iint \rho_i(\vec{u}) \rho_j(\vec{u}') e^{i \vec{s} \cdot (\vec{u} - \vec{u}')} d^3u \, d^3u',$$

where $\rho_i(\vec{u})$ is the probability of finding an atom of type i at $\vec{u}$. This expression is changed to a simpler form by use of the definition:

$$N x_i P_{ij}(\vec{r}) \equiv \int_{\substack{\text{VOL. OF}\\ \text{SAMPLE}}} \rho_i(\vec{u})\, \rho_j(\vec{u}-\vec{r})\, d^3u$$

The function $P_{ij}(\vec{r})$ is the probability of finding an atom of type j at $\vec{r}$ from an atom of type i.

The identification of $\vec{r} = (\vec{u} - \vec{u}')$, and the assumption of isotropy in a sample of radius R allows us to rewrite the equation for I(s) as:

$$I(s) = \langle f^2 \rangle + 4\pi \sum_{ij} x_i f_i f_j^* \int_0^R P_{ij}(r)\, \frac{\sin sr}{s}\, r\, dr$$

where it has been assumed that R $\gg$ interatomic distances.

By adding and subtracting the constant P_{ij}^o from the integrand, where P_{ij}^o is the average value of $P_{ij}(r)$ over the volume, we obtain:

$$I(s) - I(o) = \langle f^2 \rangle + 4\pi \sum_{ij} x_i f_i f_j^* \int_0^R (P_{ij}(r) - P_{ij}^o)\, \frac{\sin sr}{s}\, r\, dr \qquad 4.1$$

where I(o) is the so called zero scattering defined by:

$$I(o) \equiv \int_0^R P_{ij}^o\, \frac{\sin sr}{s}\, r\, dr.$$

If R is large in comparison to interatomic distances, I(o) is significant only at values of s too small to be detected experimentally. If $P_{ij}(r)$ approaches P_{ij}^o fast enough as $r \to \infty$ then the upper limit R in Eq. 4.1 can be replaced by ∞ and we have:

$$s[I(s) - I(o) - \langle f^2 \rangle] = 4\pi \sum_{ij} x_i f_i f_j^* \int_0^\infty (P_{ij}(r) - P_{ij}^o) \sin sr \, r\,dr \qquad 4.2$$

To this point the analysis has been exact, but no further progress can be made until the scattering factors are removed from the summation on the right. Using a method similar to that of Warren (6), an average electronic scattering factor, f_e, can be defined as:

$$f_e \equiv \frac{\langle f \rangle}{\langle Z \rangle}$$

Constants K_i can then be chosen such that:

$$f_i \approx K_i f_e \quad \text{and} \quad \sum_i x_i K_i = \langle Z \rangle$$

With this approximation Eq. 4.2 can be rewritten as:

$$\frac{s[I(s) - I(0) - \langle f^2 \rangle]}{\langle f \rangle^2} \simeq \frac{4\pi \sum_{ij} K_i K_j x_i}{\langle Z \rangle^2} \int_0^\infty (P_{ij}(r) - P_{ij}^o) \sin sr \, r\,dr \qquad 4.3$$

(Notice $\langle f^2 \rangle \neq \langle f \rangle^2$)

The Fourier transformation can now be applied to Eq. 4.3 with the result:

$$4\pi r^2 (P(r) - P_o) = \frac{2r}{\pi} \int_0^\infty \frac{s[I(s) - I(o) - \langle f^2 \rangle]}{\langle f \rangle^2} \sin sr \, ds \qquad 4.4$$

where $P(r)$ and P_o are defined by:

$$P(r) \equiv \frac{1}{\langle Z \rangle^2} \sum_{ij} x_i K_i K_j P_{ij}(r) \quad ; \quad P_o \equiv \frac{1}{\langle Z \rangle^2} \sum_{ij} x_i K_i K_j P_{ij}^o .$$

The term $4\pi r^2 P(r)$ is the radial distribution function, the significance of which is easily understood in the limit of random solid solution where

$$P_{ij}(r) = P_{jj}(r) = x_j P(r)$$

Thus, in this case $P(r)$ is the probability of finding an atom at a distance r from another atom and $4\pi r^2 P(r)$ is

the average number of atoms in a spherical shell, of radius r and thickness unity, centered on an atom.

Since the experimentally determined diffracted intensity, $I^E(s)$, was obtained at small scattering angles by extrapolation of the observed intensity to $I^E(s) = 0$ at $s = 0$, $I^E(s)$ can be identified as $I(s) - I(o)$. Thus, by substituting $I^E(s)$ for $I(s) - I(o)$ in Eq. 4.4 and using the experimentally determined density, P_o^E (Appendix B), the experimental radial distribution function $4\pi r^2 P^E(r)$ can be obtained from

$$4\pi r^2(P^E(r) - P_o^E) = \frac{2r}{\pi}\int_0^{s_m} \frac{s\,[I^E(s) - \langle f^2\rangle]}{\langle f\rangle^2} \sin sr\, ds \qquad 4.4a$$

where the integral is truncated at s_m, the highest value of s at which $I^E(s)$ was obtained. The function $P^E(r)$ is distinguished here from the true probability function P(r) because $P^E(r)$ necessarily contains errors caused by the truncation and by errors in $I^E(s)$. The experimentally determined radial distribution function for $Pd_{80}Si_{20}$ is shown in Fig. 4.5.

C. Errors in the Analysis. For a mono-atomic liquid Eq. 4.4a reduces to:

$$G(r) = 4\pi r(P^E(r) - P_o^E) = \frac{2}{\pi}\int_0^{s_m} s\left\{\frac{I^E(s)}{f^2} - 1\right\} \sin sr\, ds$$

It is convenient to combine all experimental errors into

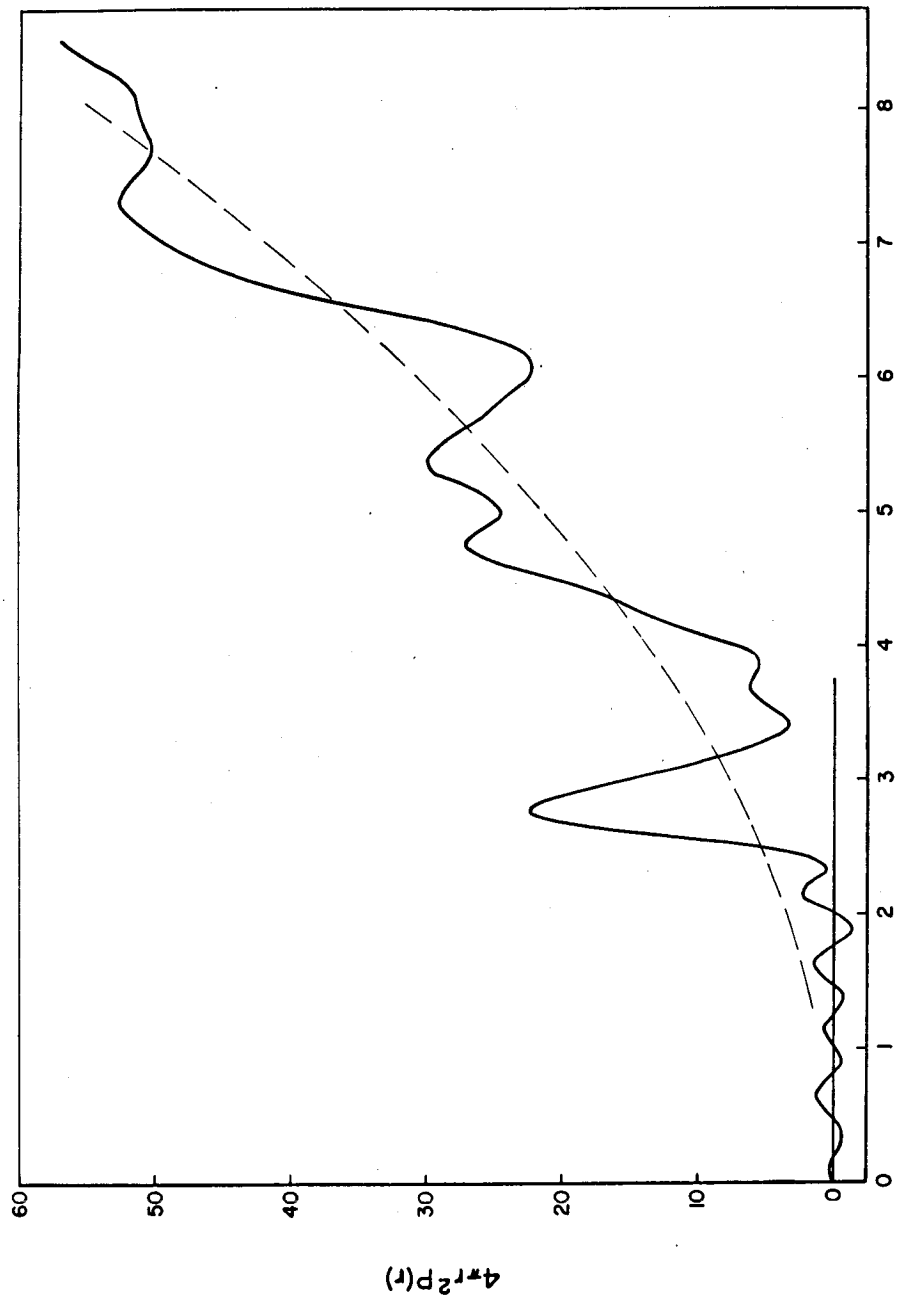

Fig. 4.5. Radial distribution function for Pd_{80} Si_{20}.

a function $\epsilon(s)$, the fractional error in $\frac{I^E(s)}{f^2}$. The error ΔG in G(r) can then be written as

$$\Delta G(r) = \frac{2}{\pi} \int_0^{s_m} s\,\epsilon(s) \left\{ \frac{I^E(s)}{f^2} - 1 \right\} \sin sr\, ds$$

$$+ \frac{2}{\pi} \int_0^{s_m} s\,\epsilon(s) \sin sr\, ds$$

If $\epsilon(s)$ is slowly varying, and $\bar{\epsilon}$ is the average value of $\epsilon(s)$, then the main effect of the first term will be to change the magnitude of G(r) by the factor $(1 + \bar{\epsilon})$. The second term will contribute an oscillatory function of periodicity $\frac{2\pi}{s_m}$ and an amplitude which varies according to the source of error (7). For example the amplitude due to errors in normalization or errors in f, is a maximum at small R. Termination of the sin transform at $s = s_m$ introduces additional ripple in G(r), or rG(r), which is a maximum in the vicinity of the first peak.

The magnitude $\Delta P(r)$ of the error in P (r) shows up most clearly at distances less than the distance of closest approach, r_c, since the true probability function P(r) vanishes for $r < r_c$. The effect of the scaling error $(1 + \bar{\epsilon})$ in G(r) and of errors in P_o will be to cause the calculated radial distribution function $4\pi r^2 P^E(r)$ to follow the curve $4\pi r^2 P_o \left(\bar{\epsilon} + \frac{\Delta P_o}{P_o}\right)$, for $r < r_c$, rather than the r axis. The ripple will occur as oscillations

about this curve. Unfortunately, the small magnitude of $4\pi r^2 \rho_o$ for $r < r_c$ causes estimation of the error $(\bar{\epsilon} + \frac{\Delta \rho_o}{\rho_o})$ to be difficult. However, in the case of $Pd_{80}Si_{20}$ (see Fig. 4.5) the ripple oscillates about the axis so closely that $(\bar{\epsilon} + \frac{\Delta \rho_o}{\rho_o})$ must be $\lesssim 0.05$.

For $Pd_{80}Si_{20}$ the ripple in $4\pi r \rho(r)$ goes through a minimum at ≈ 1 Å and reaches a maximum of 1.8 near r = 0. For $r > 1$ Å it behaves as expected for a truncation error and probably reaches another maximum at the first peak. The peak near the origin reveals that errors other than truncation are present which could, for example, include errors in the absorption and capillary corrections. In addition the approximation $f_i \approx K_i f_e$ is very poor for $Pd_{80}Si_{20}$. In the range $0 \leq s \leq 15$, $\frac{f_{Pd}}{f_e}$ varies by 1.5% and $\frac{f_{Si}}{f_e}$ by almost 30%. Nevertheless, it is probably true that except in the vicinity of the first peak, errors in the radial distribution function shown in Fig. 4.5 are comparable in magnitude to the ripple at $r < 2$ Å.

Thus, the phase and magnitude of the small peak at 3.65 Å in Fig. 4.5 suggests that it is entirely due to ripple. The dip at 5 Å is probably a true feature of the radial distribution function, but because of its small size it must be significantly affected in position and magnitude by the ripple.

D. Discussion. The diffraction pattern shown in Fig. 4.4 is similar in form to those obtained from liquid metals. An interesting feature, which also appears in the electron diffraction patterns of the previous chapter, is the shoulder on the high angle side of the second peak. It is also characteristic of a nickel phosphorous alloy studied by Dixmier and Doi (8). The diffraction pattern of the NiP alloy by its close resemblance to that of 20 at. % Si, Pd, indicates a similar structure for the two alloys. In neither case was it found possible to explain the observed diffraction on the basis of a structure of fcc, bcc or hcp microcrystals.

The radial distribution function shown in Fig. 4.5 is similar to those of liquid metals although the density variations are more pronounced. In particular the initial peak is somewhat sharper and more isolated (although not larger in area) than those of most close packed liquids. This is not surprising since it has been observed before that the radial distribution function of a glass has sharper features than that of the corresponding liquid (9). Experimental radial distribution curves of amorphous metal foils deposited by vapor deposition also seem to exhibit considerable resolution of detail as compared to the corresponding liquids (10).

The second coordination shell is split, unlike a liquid, at r = 5 Å. Similar detail has been observed by Richter, et al, in the radial distribution functions of amorphous metal film (10). However, this work has been severely criticized and it is not clear how much reliance should be placed upon these results. Since this feature is not much larger than the error expected from the Fourier ripple, it is probably fruitless to speculate upon its significance. The general shape of the function is not unreasonable and may be taken as evidence for a liquid like structure in 20 at. % Si,Pd.

It is of interest here to remark upon the results of Dixmier and Doi on nickel-phosphorous alloys. Their radial distribution curve was similar to the one for 20 Si, Pd but exhibited much more pronounced variations. In particular, the peak between the first and second main peaks, was significant. The splitting of the second main peak was much more pronounced and there were more minor peaks at higher distances. On the basis of this "unreasonable" result they concluded that the structure of the alloy consisted of a random packing of hexagonal planes. By using the theory (with several adjustable parameters) of diffraction from an array of randomly packed planes of atoms (11), they calculated a theoretical diffraction pattern which was quite similar to the experimentally determined pattern. Without further evidence of a layered structure, however, the result is not

convincing. Such an approach might have been applied here but the experimental results did not appear to justify it.

One possibility not mentioned so far is that of a segregation of the alloy into two glass phases such as is often observed in some silica-base glasses. Alternatively, an ordering of the component atoms could occur. Either of these possibilities could result in a splitting of the observed coordination shells. The observed splitting, being small in magnitude and not occurring in the first peak is not sufficient evidence that either of these possibilities occur here. Due to the fact that the atomic sizes of Si and Pd are nearly equal, these effects could easily go undetected.

In the absence of evidence to the contrary, the distribution was assumed below to be a random solid solution for the purpose of estimating coordination numbers. Geometrical data taken from the distribution curve is presented in Table 4.2. Coordination numbers and atomic shell distances for fcc Pd are given for purpose of comparison. The distance of closest approach, 2.79 Å, is in good agreement with the Pauling atomic diameters 2.75 Å and 2.77 Å for Si and Pd respectively. That the short range order of Pd is preserved in the glass is indicated by the value 11.6 for the first coordination. number. This fact may be important in accounting for the

observed precipitation from the glass of a face centered cubic phase. The density difference (see Appendix B) between amorphous and crystalline states probably arises as a consequence of a loss in long range order.

TABLE 4.2

Comparison of the Structures of

Amorphous $Pd_{80}Si_{20}$ and Pure Palladium

$Pd_{80}Si_{20}$ Glass		Palladium	
Shell Distance	Coord. Number	Shell Distance	Coord. Number
2.79 Å	11.6	2.77 Å	12
4.78 Å		3.89 Å	6
5.38 Å		5.50 Å	12

REFERENCES

1. R. F. Kruh, Chem. Rev., 62, 319-346, (1962).
2. H. H. Paalman and C. J. Pings, J. Appl. Phys., 33, 2635-2639, (1962).
3. R. W. James, The Optical Principles of the Diffraction of X-rays, 462-463, (1962).
4. L. Bewilogua, Phys. Z., 32, 740-744, (1931).
5. J. Krogh-Moe, Acta. Cryst., 9, 951-953, (1956).
6. B. E. Warren, H. Krutter and O. Morningstar, J. Am. Ceram. Soc., 19, 202-206, (1936).
7. R. Kaplow, S. L. Strong, B. L. Averbach, Phys. Rev., 138, A1336-A1345, (1965).
8. J. Dixmier, K. Doi, and A. Guinier, Physics of Non Crystalline Solids, 36-48, (1965).
9. K. Furakawa, Reps. Prog. in Phys., 25, 395-440, (1962).
10. H. Richter and S. Steeb, Z. Met., 50, 369-374, (1959).
11. A. J. C. Wilson, Acta. Cryst., 2, 245-251, (1949).

V. CRYSTALLIZATION OF AMORPHOUS $Pd_{80}Si_{20}$

A. Introduction. The glass phase of any alloy will crystallize if heated to a sufficiently high temperature. Previously published results indicate that when amorphous $Pd_{80}Si_{20}$ foils are heated at rates between 20°C/min. and 10,000°C/min., the crystallization takes place suddenly at 400°C ± 10°C with a heat release of 1 k. cal/g. atom (1). This large heat evolution, which is of the order of magnitude of the heat of fusion of metals, can be regarded as indirect evidence that the quenched $Pd_{80}Si_{20}$ foils are amorphous. The heat of fusion of this alloy is unknown but is expected to be larger than 1 k. cal/g. atom because (see Chapter III) the heat capacity of an undercooled liquid is greater than that for the crystalline solid in the same temperature interval.

The transformation "burst" at 400°C does not imply that the devitrification of $Pd_{80}Si_{20}$ takes place at a sharply defined temperature. In fact at heating rates much below 20°C/min. the transformation is complete before the temperature reaches 400°C. Rather, 400°C is probably the temperature at which the reaction is fast enough to enable the heat of crystallization to overcome heat losses and cause the reaction to become self sustaining.

A study of the devitrification kinetics can be best carried out by following the progressive change in the x-ray diffraction pattern as foils of the amorphous alloy are held at different temperatures. Studies using this approach are presently being carried out at this laboratory. Another method for studying the devitrification is to follow the progressive change in physical properties of the alloy as the transformation proceeds. This chapter is concerned with the results of following the transformation by measuring the electrical resistance of the devitrifying alloy. Two experimental approaches were used. In the first, the resistance of the alloy was measured as it was heated at a constant rate of about 1.5°C/min., while in the second resistance measurements were made on foils transforming at constant temperatures of 286.5°C, 313°C and 346°C respectively.

B. Experimental Procedure. All resistance measurements were conducted using the null circuit shown in Fig. 5.1. In this method the unknown resistance is determined by comparing the voltage drop across it to that across a precision standard resistance when a constant current ($\approx$0.1 amps.) is applied to both. Adjustment for thermal emf in the circuit was accomplished by reversing the polarity.

The apparatus illustrated in Fig. 5.2 was used in the

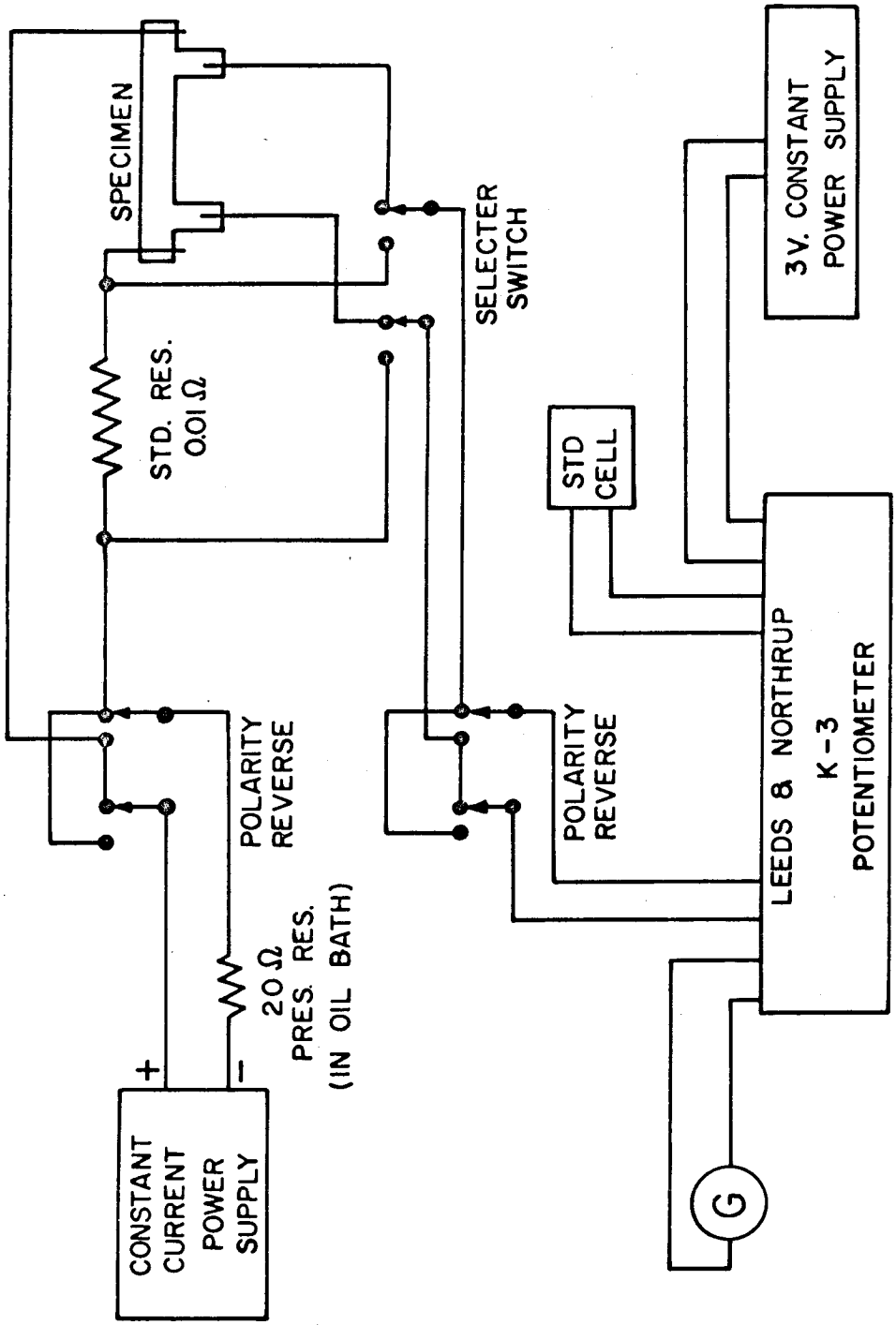

Fig. 5.1. Null circuit for measurement of electrical resistance.

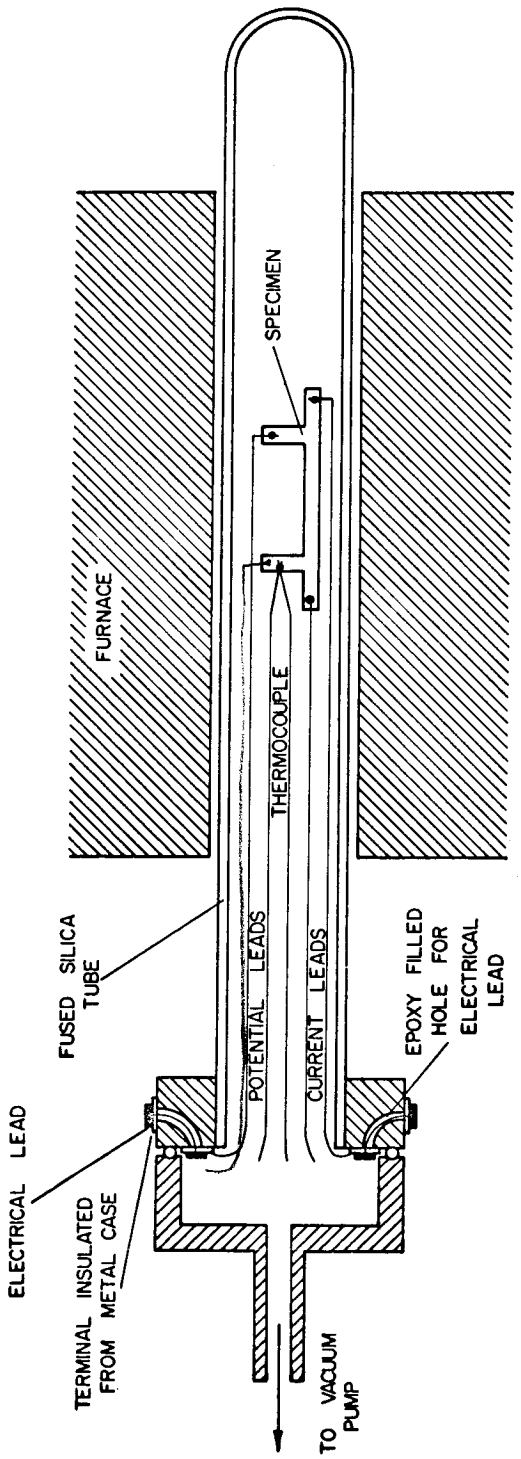

Fig. 5.2. Apparatus for maintaining foil specimens in a vacuum while measuring their electrical resistance at temperatures of up to 800°C.

measurement of the resistance of $Pd_{80}Si_{20}$ foils at temperatures up to the melting point. The foil specimen, machined to the shape shown in Fig. 5.2, was supported in the evacuated fused silica tube by the spotwelded chromel electrical leads and chromel alumel thermocouple. As indicated in Fig. 5.2 the electrical leads were spotwelded to current and potential ears on the specimen in such a way that regions in the vicinity of the spotwelds did not contribute to the resistivity.

Foils produced by the "gun" method were annealed and examined with the electron microscope. Annealing was done either on a specimen hot stage inside the microscope or in sealed pyrex tubes which were evacuated to 10^{-6}mm. of mercury and gettered with yttrium.

C. Results. The resistance of four specimens was measured while heating them at a constant rate of 1.5°C/min. The resistivity, which is plotted in Fig. 5.3, was calculated by a method to be explained in the next chapter. The dashed line in Fig. 5.3 shows the resistivity of the specimens after being annealed 75 hours at 750°C. It is apparent from the figure that devitrification is detectible, for this rate of heating, at about 350°C. The depression of the resistivity curve between 400°C and 535°C indicates that the amorphous $Pd_{80}Si_{20}$ first transforms to a metastable state which in turn transforms to the equilibrium state

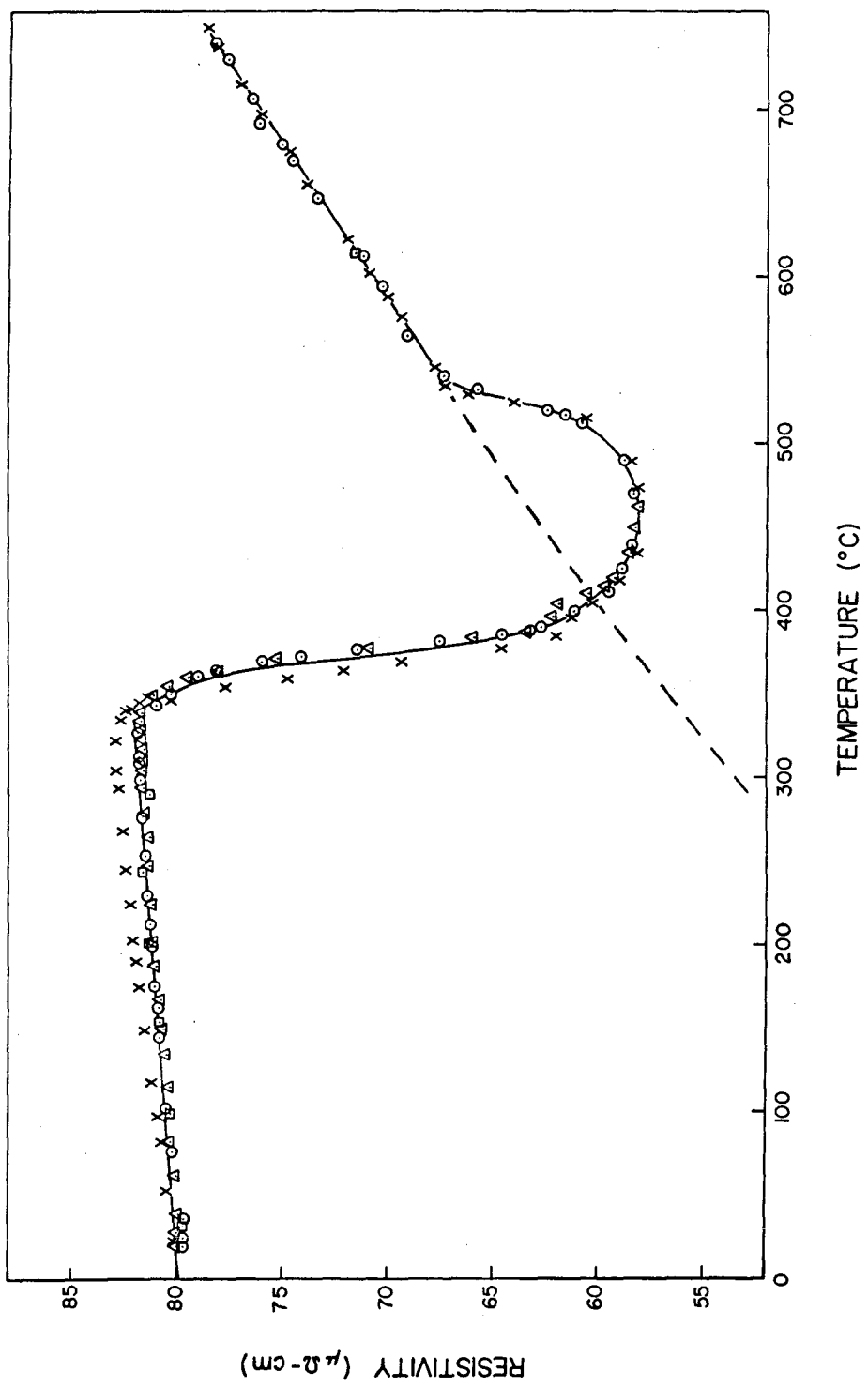

Fig. 5.3. Change in the electrical resistivity of initially amorphous $Pd_{80}Si_{20}$ foils during heating at a constant rate of 1.5°C/min.

beyond 535°C.

The transformation of the amorphous $Pd_{80}Si_{20}$ foils to the metastable crystalline state was studied by measuring the electrical resistance, R(t), of several foils as a function of the time t as they were maintained at temperatures of 286.5°C, 313°C or 346°C ± 1°c. Warm up time, which was uncorrected for, was kept to less than three minutes by plunging the specimens into the preheated furnace. The fact that in most cases no nucleation period was observed when R(t) was plotted versus time indicates that the crystal growth proceeded from pre-existing nuclei in the amorphous matrix.

Transformation curves are shown in Fig. 5.4 where each point represents an average of determinations of the relative resistance $\frac{R(t)}{R(0)}$ upon several samples and R(0) = initial resistance. To facilitate comparison between the transformation at different temperatures, the relative resistance was corrected to 286.5°C by using the measured temperature coefficients of resistivity for the glass and the metastable crystalline state. It was assumed that for intermediate stages of transformation the coefficient varied linearly with the change in relative resistance. The error introduced into calculations of the activation energy by neglecting this correction is less than 1%.

For a diffusion controlled process the transformation

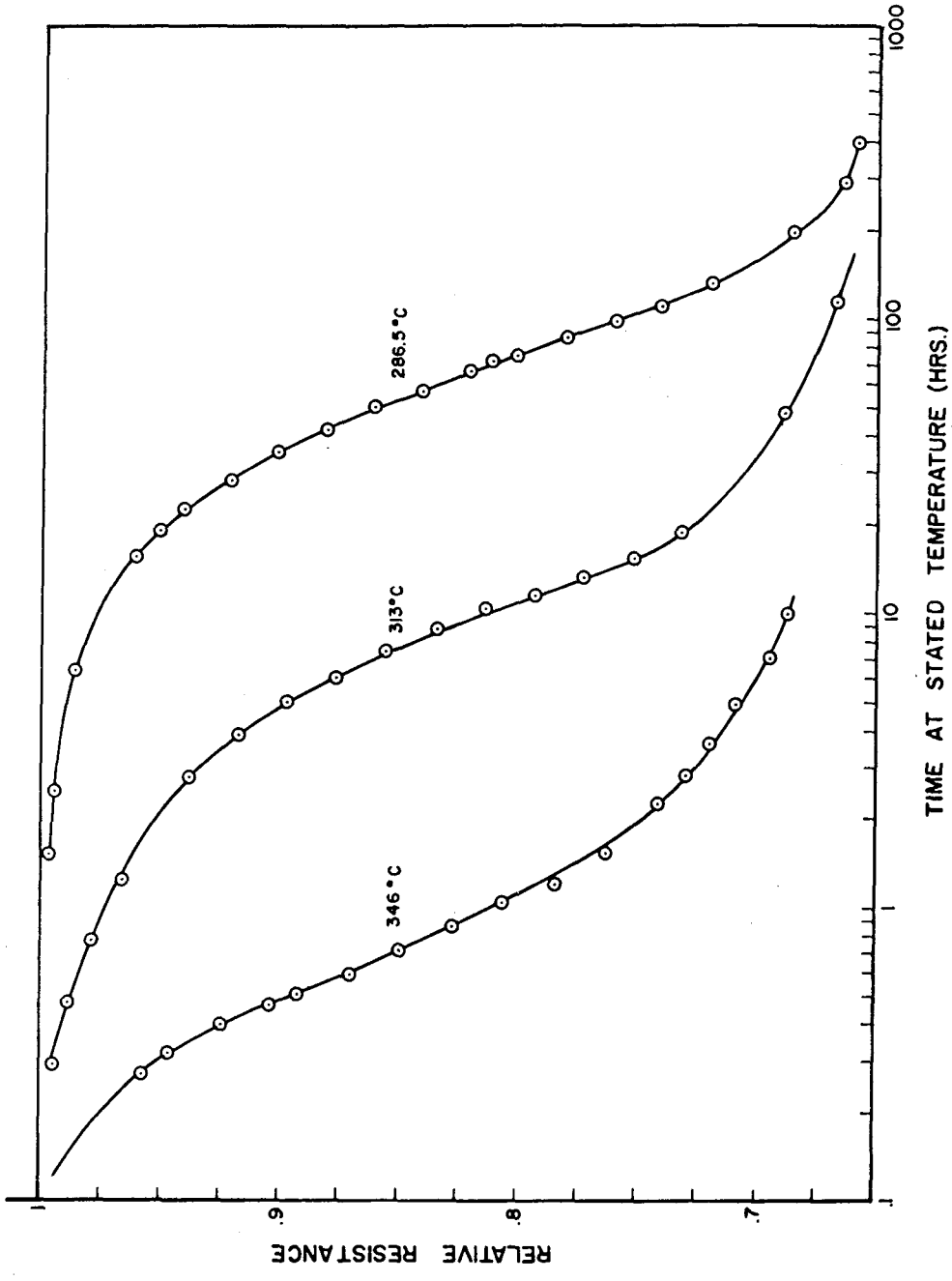

Fig. 5.4. Experimentally determined variation of electrical resistance with amount of heat treatment of initially amorphous $Pd_{80}Si_{20}$ foils.

rate, P, is given by:

$$P = C \exp\left\{\frac{-Q}{RT}\right\}$$

where Q is the activation energy, T is the absolute temperature (^{o}K), R is the gas constant (1.987 cal/^{o}K) and C is a constant with respect to temperature. If the rate P is identified as the reciprocal of the time t required for

to attain a specific value, then an activation energy Q can be calculated for the resistance change from:

$$Q = 2.303 \frac{d \log_{10} t}{d\left(\frac{1}{T}\right)}$$

Graphs used for this purpose are given in Fig. 5.5 and values of Q calculated for different values of $\frac{R(t)}{R(0)}$ are presented in Table 5.1.

TABLE 5.1

Activation Energy for Transformation of the Amorphous Solid

Relative Resistance	Activation Energy
0.95	49.02
0.90	49.05
0.85	50.31
0.80	49.05
0.75	46.22

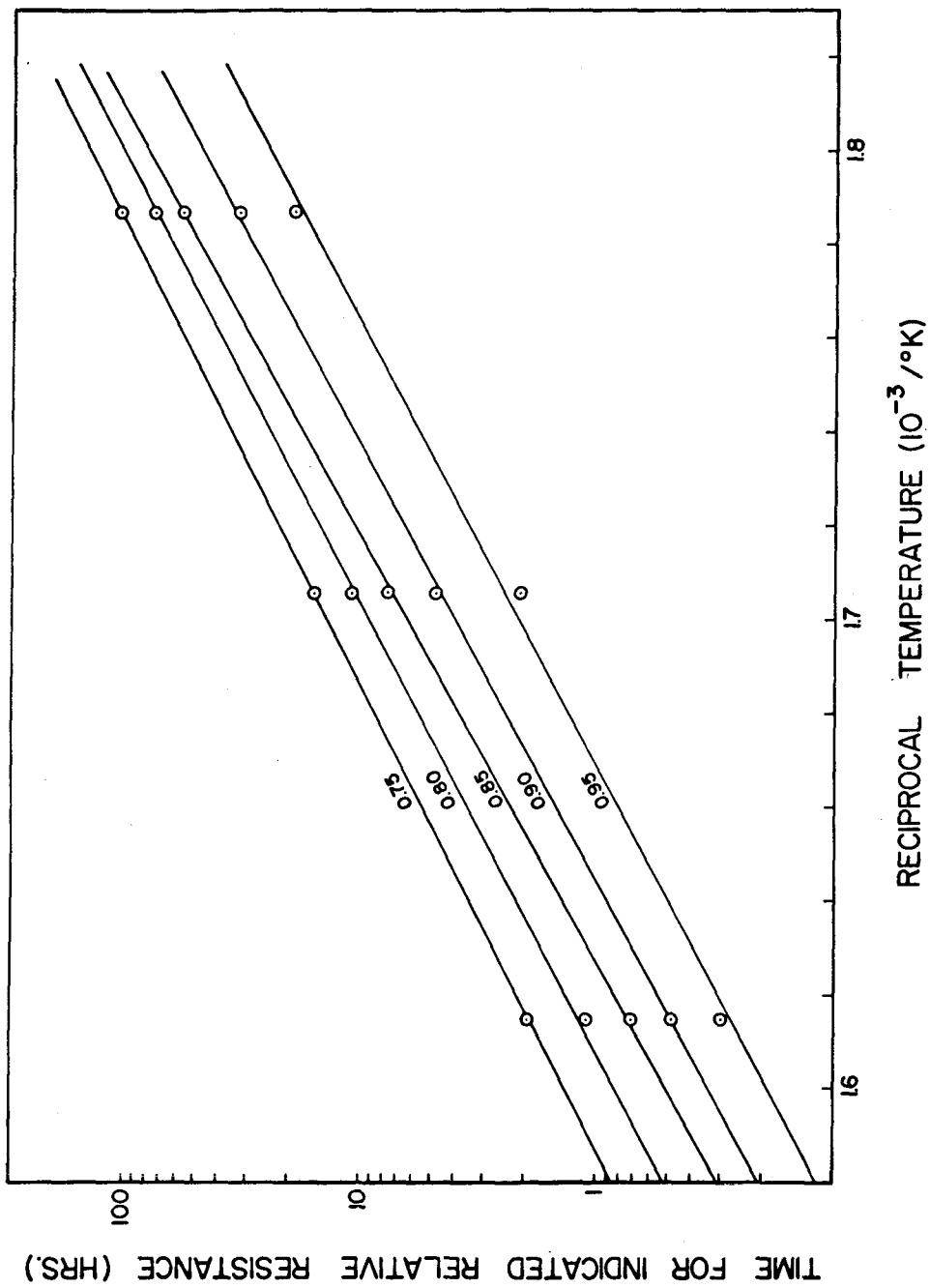

Fig. 5.5. Graph for the determination of Q for Pd_{80} Si_{20}.

Since the relative resistance $\frac{R(t)}{R(0)}$ is not related in a known way to the amount of transformation a detailed analysis of the results was not attempted. However, if the product of the transformation is independent of temperature (over the range considered), then the activation energy for the transformation should be the same as that calculated from the resistance measurements.

The most significant fact about the devitrification, as observed by electron microscopy, is that a face centered cubic phase and one or more silicides precipitate independently of one another. An example is shown in Fig. 5.6 where the quenched foil of Fig. 5.6a was heated in the microscope for ten hours at $\approx 270^{\circ}C$ to cause the crystallization shown in Fig. 5.6c. In this micrograph a silicide (or mixture of silicides) has crystallized on a front while the fcc phase (as indicated by the selected area diffraction pattern of Fig. 5.6d) has precipitated in individual crystals. A few of the fcc crystals are barely visible in Fig. 5.6a and it is likely that all were present as nuclei in the quenched foil. Their diffraction pattern, however, does not exhibit the preferred orientation which would be expected on the basis of results with alloys of lower Si concentrations.

It is interesting to note that the fcc phase is metastable in the alloy $Pd_{80}Si_{20}$. In addition, the diffraction patterns of the observed silicides do not match that

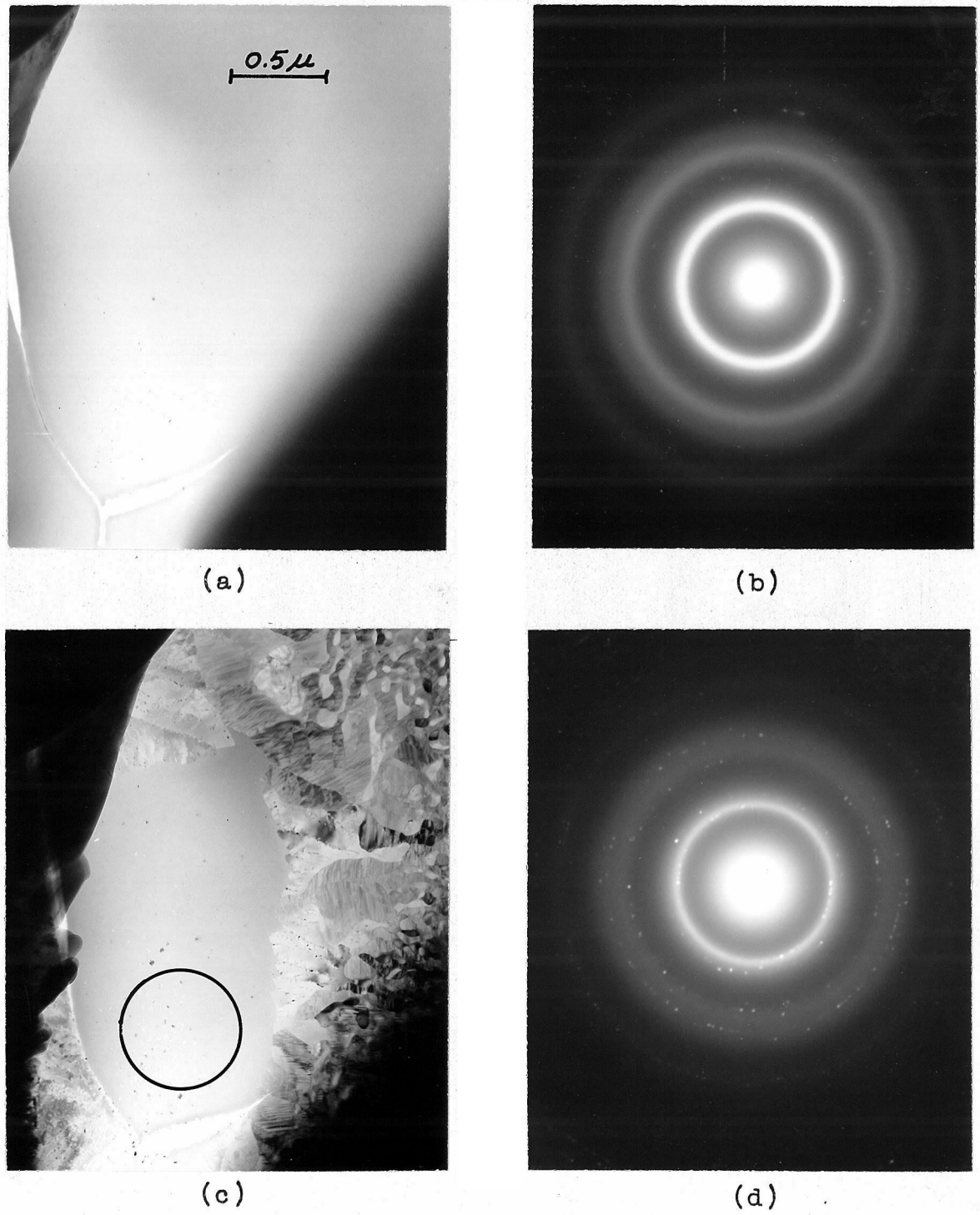

Fig. 5.6. (a) Transmission electron micrograph of a quenched $Pd_{80}Si_{20}$ alloy. (b) Selected area electron diffraction pattern of region shown in (a). (c)Region of foil shown in (a) after heating it on the microscope hot stage for 10 hours at approximately 270°C. (d) Selected area electron diffraction pattern from the area circled in (c).

expected for Pd_3Si. Since preliminary results (2) of following the transformation by x-ray analysis indicate that the relative amounts of the various precipitating phases depend upon the transformation temperature, it is clear that the above activitation energy does not have an easily interpreted significance. The transformation is complicated by the fact that the metastable silicide is unstable relative to the fcc phase which grows at its expense when the phases are in contact.

Other micrographs, showing the silicide (or silicides) crystallizing at a front are shown in Fig. 5.7 and 5.8. Fig. 5.7d, a diffraction pattern of the crystallized region of Fig. 5.7b, indicates the presence of a residual amount of the amorphous phase.* This is often observed and may be due to crystallization which initially occurs only on the surface of the foil. In many cases the crystallized regions have the appearance of a lamellar eutectic (Fig. 5.8). Alternate lamelle appear to have the same crystallographic orientation and may belong to the same crystal. The fcc phase is not present in this micrograph and the lamelle all appear to belong to a single silicide.

---

* In this case the uncrystallized region was close enough to the selector aperture that it may have contributed to the amorphous diffraction pattern.

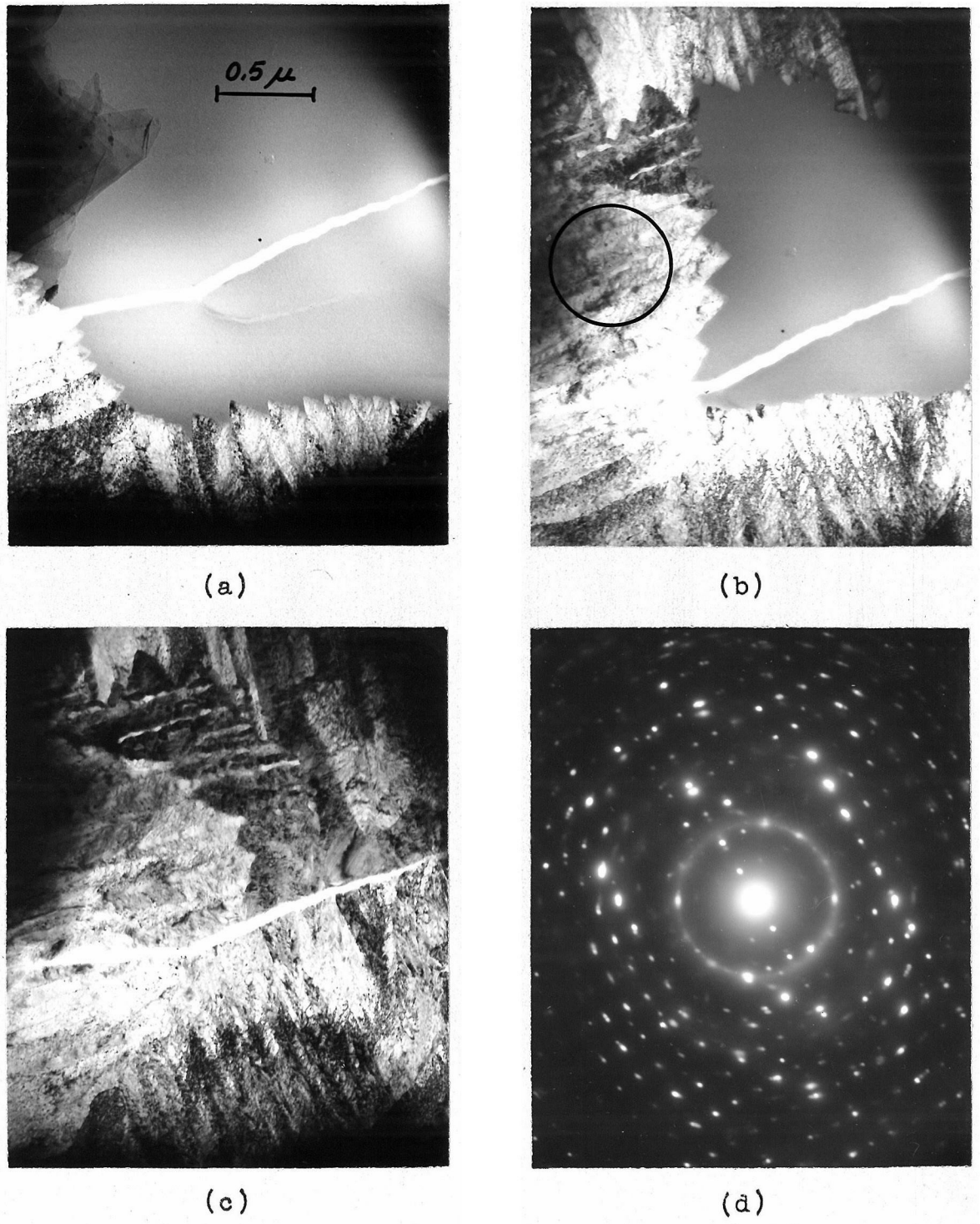

Fig. 5.7. Transmission electron micrographs of a quenched $Pd_{80}Si_{20}$ foil after being heated at approximately 270°C on the microscope hot stage for (a) 1.5 hours (b) 5 hours (c) 10 hours. (d) Selected area electron diffraction pattern from the region circled in (b). (100 kV.)

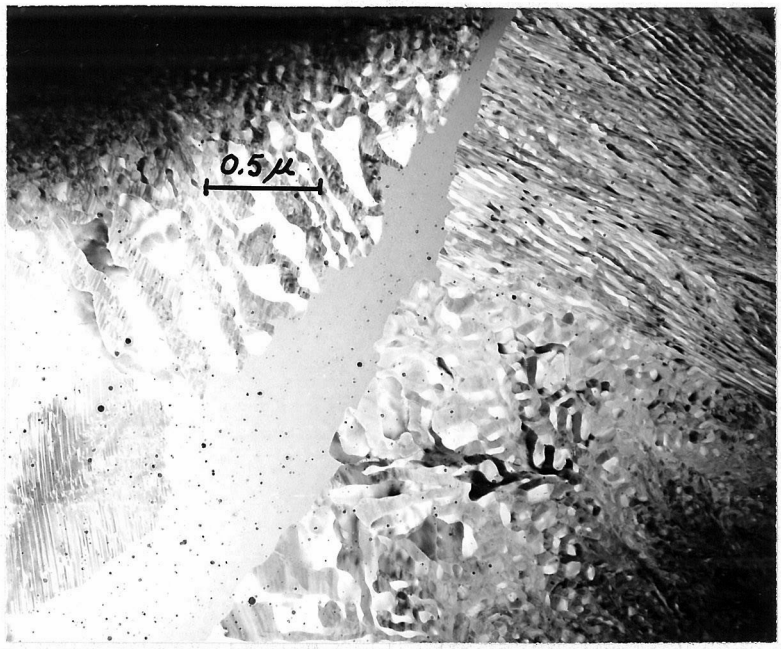

(a)

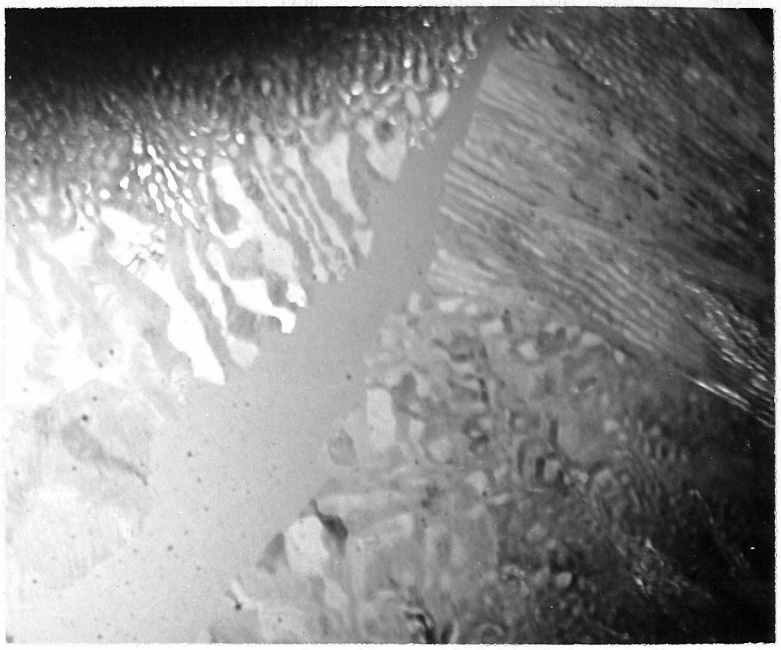

(b)

Fig. 5.8. (a) Transmission electron micrograph of a $Pd_{80}Si_{20}$ foil annealed 35 minutes at approximately 285°C on the microscope hot stage. (b) Dark field electron micrograph of the same region, obtained by placing the objective aperture over one of the low angle crystalline diffraction spots. (100 kV.)

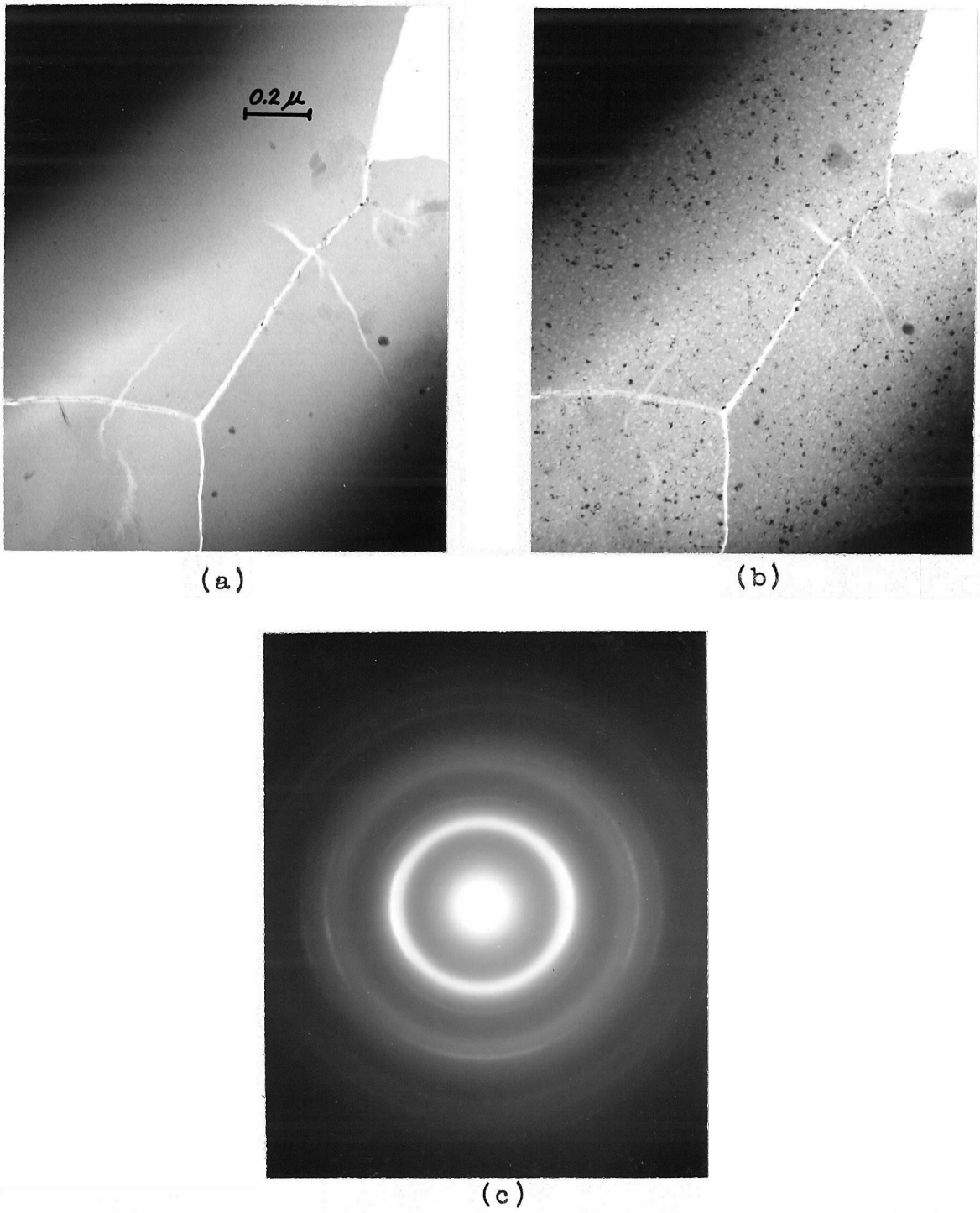

Fig. 5.9. Transmission electron micrograph of a quenched $Pd_{80}Si_{20}$ foil before (a), and after (b) annealing it on the microscope hot stage for 45 minutes at approximately 275°C. (c) Selected area diffraction pattern from the partly crystallized region shown in (b). (100 kV.)

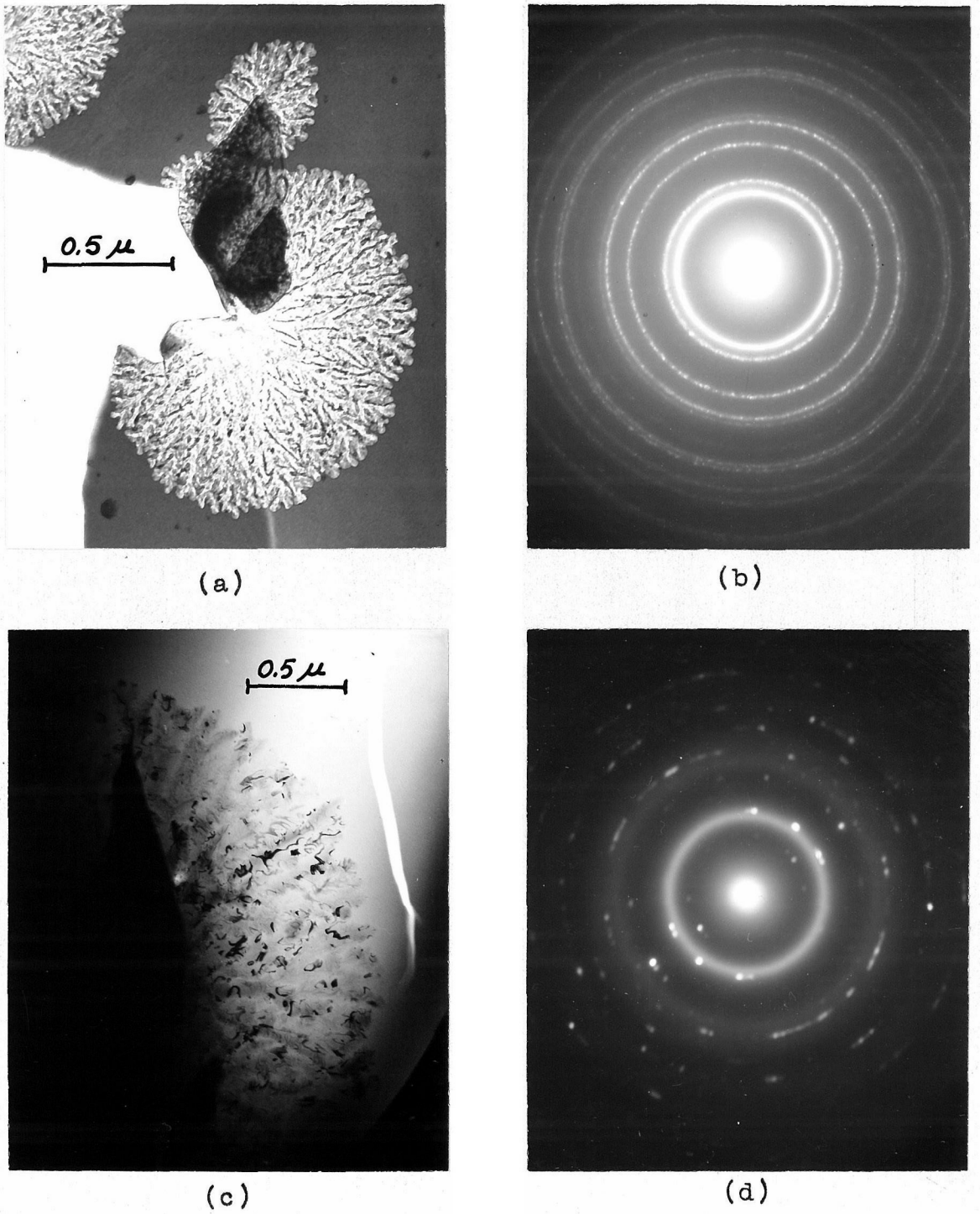

Fig. 5.10. Spherulites found in $Pd_{80}Si_{20}$ foils annealed in evacuated Pyrex tubes for 6 hours at 285°C. (a) Spherulites composed of fcc crystals. (b) Selected area diffraction pattern from a spherulite shown in (a). (c) Spherulite composed of crystals of an unknown structure. (d) Selected area diffraction pattern from the spherulite shown in (c). (100 kV.)

The silicides do not always crystallize on a front and, as shown in Fig. 5.9, sometimes appear as isolated single crystals. Occasionally spherulites of an fcc or more complicated structure are observed, as in Fig. 5.10, in the annealed foils.

REFERENCES

1. Pol Duwez, R. H. Willens and R. C. Crewdson, J. Appl. Phys., 36, 2267-2269, (1965).

2. Pol Duwez, private communication.

VI. RESISTIVITY OF THE LIQUID, GLASS AND CRYSTALLINE PHASES OF $Pd_{80}Si_{20}$

A. Experimental Procedure. A fused silica U tube (Fig. 6.1), calibrated with liquid mercury, was used with the measuring circuit described in Chapter V to measure the resistivity of liquid PdSi alloys. Approximately thirty grams of the solid alloy was placed in the U tube at "A" in Fig. 6.1, melted under a vacuum of approximately 25μ, and then forced into the fused silica capillaries by argon which was released into the center tube. By maintaining a temperature gradient in the four PdSi "electrical leads" between B or B' and the tungsten wire tips such that the tungsten never exceeded 650°C, it was possible to obtain electrical contact between the tungsten and the molten alloy without contaminating the alloy. This was possible because the liquid solidified soon after making contact with the tungsten and prevented it from dissolving. By using two of the four electrical leads to supply current and two to measure electric potential, the resistance of the liquid in Section BB' was measured. In the region of the furnace containing Section BB' the temperature was constant to within $\pm$ 1°C as a result of a nickel liner in the bottom half of the furnace. The temperature of the liquid at "A" was measured with a Cr-Al thermocouple protected by a fused silica sheath.

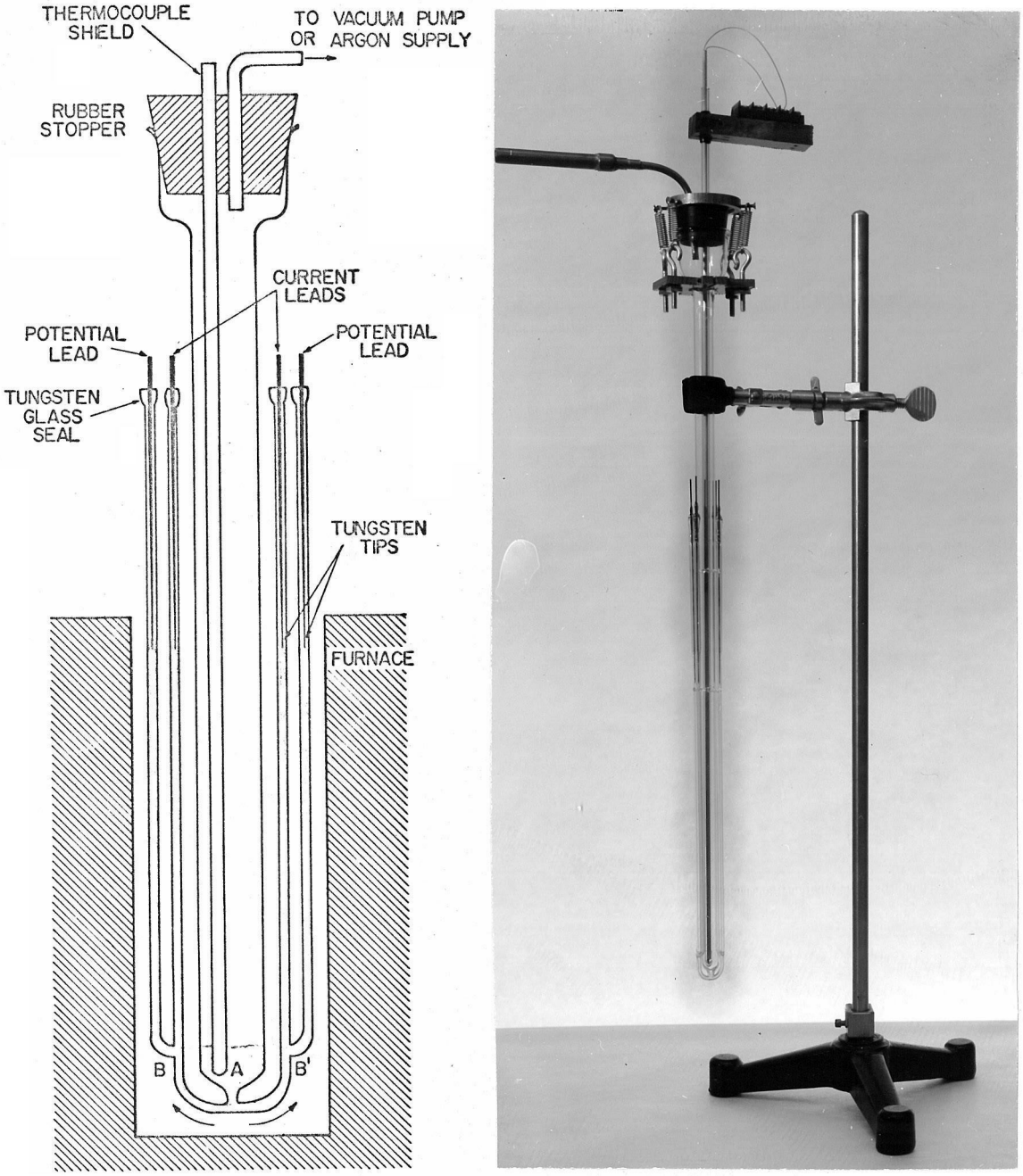

Fig. 6.1. Schematic diagram and photograph of the U-tube apparatus used in the measurement of the electrical resistivity of liquid PdSi alloys.

The resistivity of liquid $Pd_{80}Si_{20}$ as determined by two samples is shown in Fig. 6.2. The thermocouple used for sample No. 1 was, on subsequent calibration, found to have a temperature uncertainty of $\pm$ 15°C which is probably the cause of the small discrepency in the results for the two specimens. Other thermocouples used in this investigation were found to be high by 5°C $\pm$ 2°C when calibrated with a standard thermocouple at 1000°C. In order to determine the dependence of the resistivity on the Si concentration, the resistivity of a specimen of molten $Pd_{83}Si_{17}$ was also measured (Fig. 6.3).

The major problem in using the U tube method to measure resistivity is related to the transition between solid and liquid, which is present in the four electrical leads. The possibility of solute rejection as the interface moves during temperature changes causes an uncertainty in the composition of the remaining liquid, which could affect both the magnitude and the temperature coefficient of the measured resistivity. The reservoir of excess liquid at "A", which constituted 85% to 90% of the total alloy, served to minimize changes in the average composition. In addition the melt was kept at a constant temperature for several hours before the measurement in order to allow composition gradients in the liquid to dissipate.

When the liquid in BB' is at temperatures above the

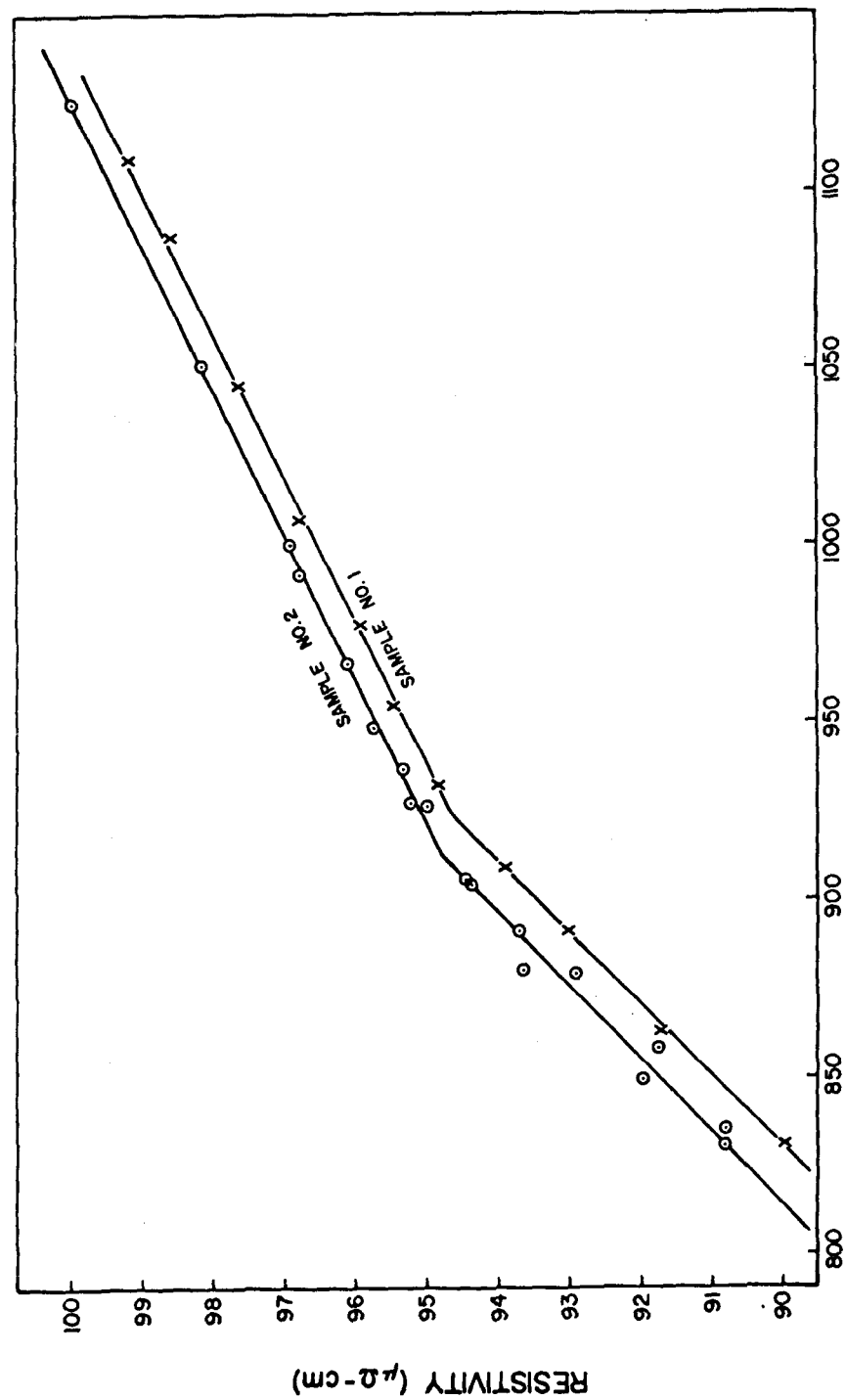

Fig. 6.2. Electrical resistivity of liquid $Pd_{80}Si_{20}$, as determined from measurements upon two samples.

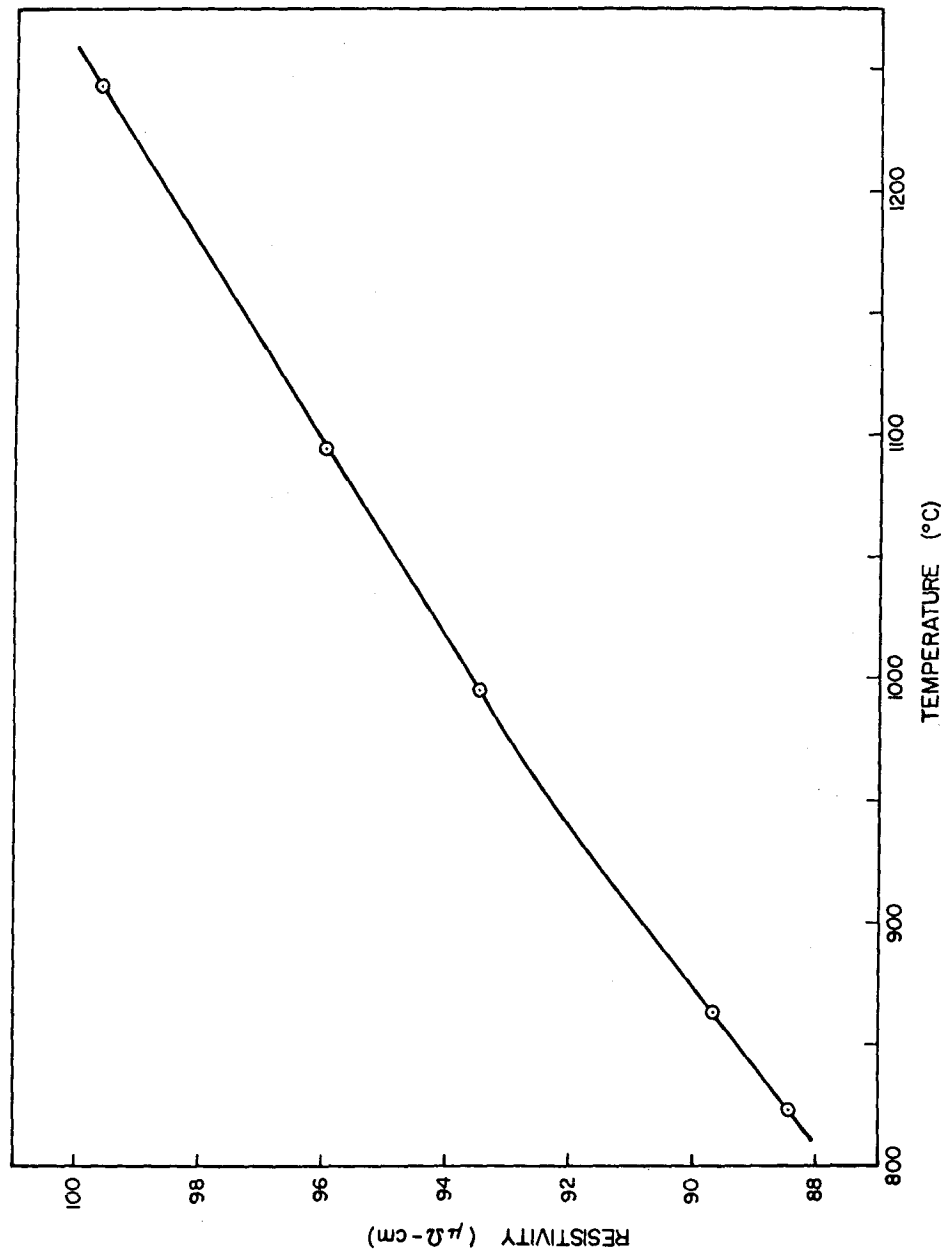

Fig. 6.3. Electrical resistivity of liquid $Pd_{83}Si_{17}$.

liquidus, it is easy to estimate the maximum uncertainty in ρ and in $\left(\frac{\partial \rho}{\partial T}\right)_P$ due to solute rejection. If it is assumed that the temperature in the electrical leads varies linearly between 650°C and 915°C when the liquid in BB' is at 915°C, the change in average composition of the liquid caused by the solidification of pure Pd_3Si is only 0.4 at. % Si. Since $\rho = 96.9\ \mu\Omega\text{-cm}$ for liquid $Pd_{80}Si_{20}$ at 1000°C, and $93.6\ \mu\Omega\text{-cm}$ for liquid $Pd_{83}Si_{17}$; $\left(\frac{\partial \rho}{\partial c}\right)_{P,T} = 110\ \mu\Omega\text{-cm}$ where c = mol fraction of Si. Thus, the maximum change in the magnitude of ρ due to solute rejection is $\approx -0.4\ \mu\Omega\text{-cm}$. If it is assumed that the maximum variation of composition is half of this (or 0.2 at. %) as the temperature varies between 916°C and 1200°C, then the maximum change in $\left(\frac{\partial \rho}{\partial T}\right)_P$ due to this effect is only $-0.12 \times 10^{-2}\ \mu\Omega\text{-cm}/^{\circ}C$. This compares to $\left(\frac{\partial \rho}{\partial T}\right)_P = 2.49 \pm 0.06 \times 10^{-2}\ \mu\Omega\text{-cm}/^{\circ}C$ calculated from the slope of $\rho(T)$ above the liquidus temperature (Fig. 6.2).

There is also experimental evidence that errors in the resistivity of the liquid due to solute rejection may be negligible. When the entire sample finally solidifies, section BB' should experience the maximum deviation from the average composition. However, as shown in Fig. 6.5, resistivity data from sample No. 2 taken in the temperature range between 700°C and 800°C after solidification occurred, matches the resistivity of an equilibrium specimen (to be described below). Thus, it is concluded that errors in ρ

and $\left(\frac{\partial \rho}{\partial T}\right)_P$ due to solute rejection are negligible for the purposes of this investigation.

In order to measure the resistivity of the equilibrium crystalline alloy, two specimens like that in Fig. 6.4b were cast in a fused silica U tube (Fig. 6.4a) previously calibrated with liquid mercury. In order to avoid undercooling of the melt, the cast specimens were inoculated with $Pd_{80}Si_{20}$ chips at the liquidus and solidus during slow cooling from the melt. The specimens were subsequently annealed seventy five hours at 750°C. To guard against specimen damage due to stress from the unequal thermal contraction of the specimen and the fused silica, the mold was previously weakened so that it shattered easily at about 700°C. Oxidation of the specimen at this point was prevented by maintaining an argon atmosphere about the specimen and mold. The possibility of errors in the resistivity caused by solute rejection during solidification was checked by making resistivity measurements upon different sections of the specimen. No significant differences were found. In addition no flaws, which were capable of significantly altering the resistance, were found upon the surface of the specimens. The results of measurements upon the two specimens are shown in Fig. 6.5 along with data obtained from the solidified specimen No. 2 used to measure the resistivity of the liquid.

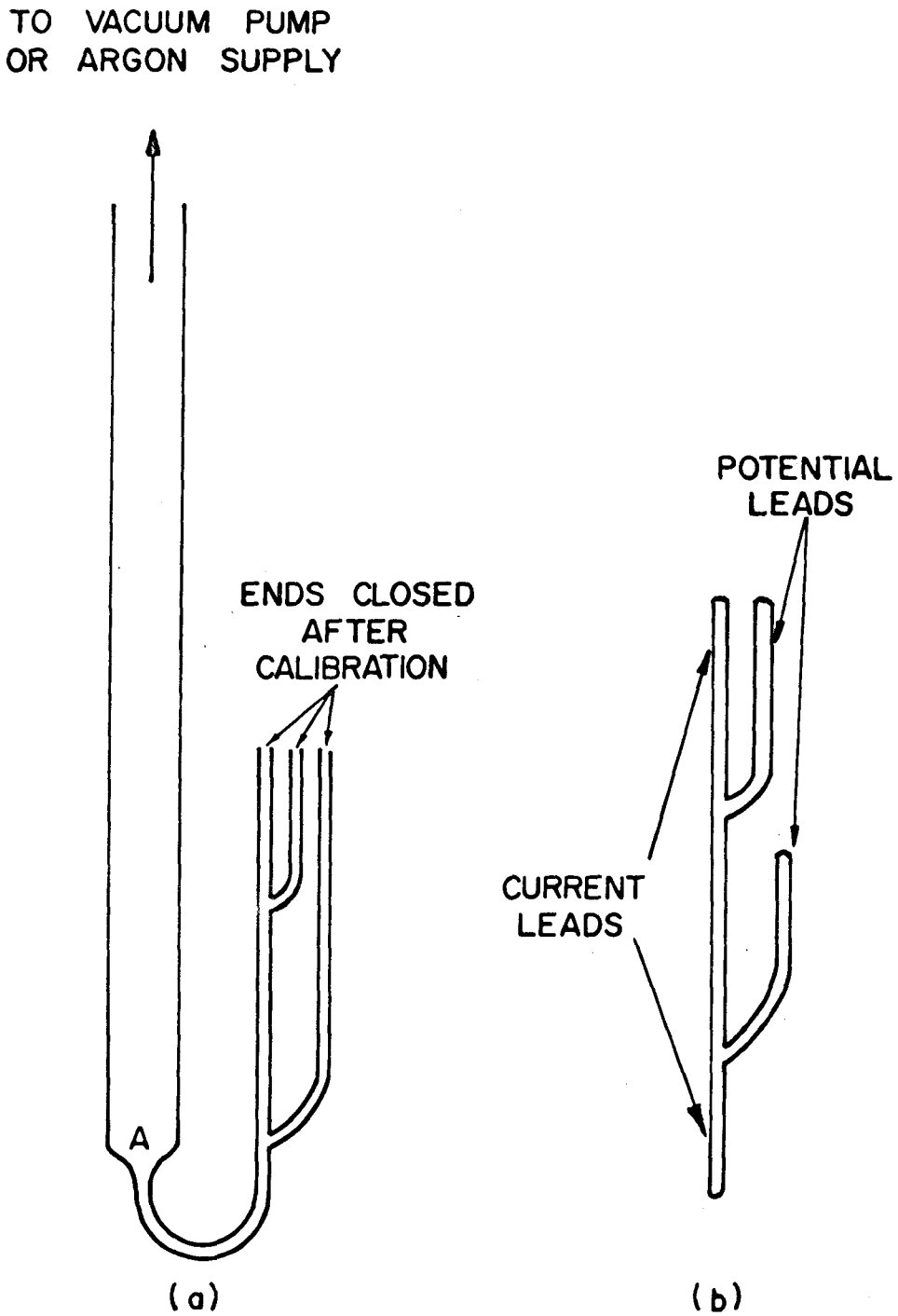

Fig. 6.4 (a). Fused silica U-tube used to cast the electrical resistivity specimen shown in (b).

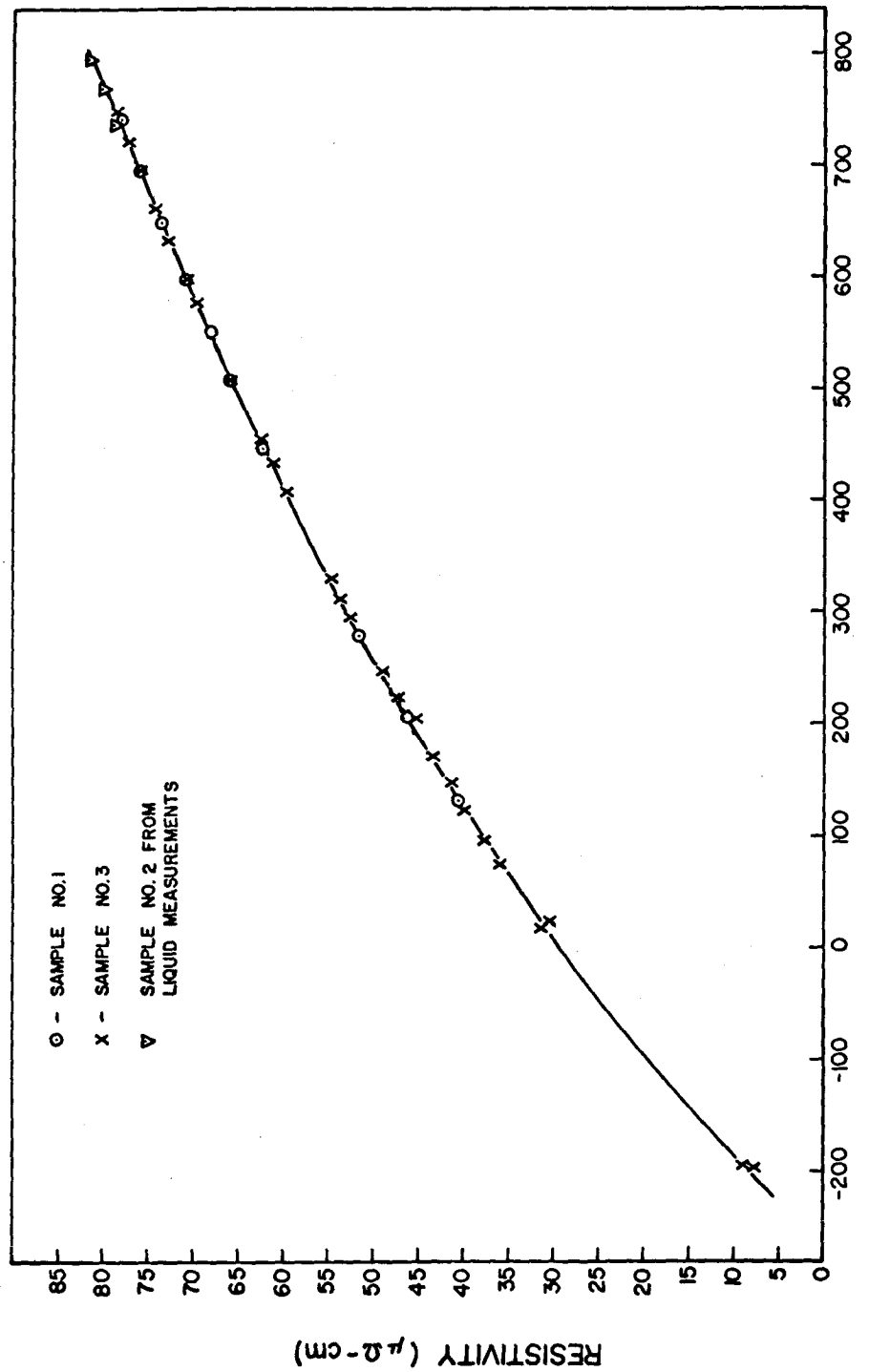

Fig. 6.5. Resistivity of cast $Pd_{80}Si_{20}$ specimens #1 and #3 after they were annealed for 75 hours at 750°C. For comparison, the resistivity obtained from liquid sample #2, after its solidification, is also plotted.

The resistivity of the foils used in the constant heating rate experiments (Fig. 5.3) was calculated on the assumption that after being annealed seventy five hours at 750°C, they had the same resistivity as the cast and annealed specimens discussed above. The validity of this method is supported by the fact when the resistivity of the annealed foils is normalized to that of the cast specimens at a single temperature, the matching is good over a wide temperature range (Fig. 6.6). The average resistivity of the amorphous foils calculated in this manner (and corrected for thermal expansion) is 79.4 ± 0.5 $\mu\Omega$-cm at 20°C. This compares with the value 82.7 ± 3.4 $\mu\Omega$-cm calculated from the dimensions and resistance of the 15 foils used in Chapter V.

Values of the temperature coefficient of the resistance, $\frac{1}{R}\left(\frac{\partial R}{\partial T}\right)_P$, at 20°C ranged from 0.90 x 10^{-4} to 3.31 x 10^{-4} for the fifteen amorphous foils studied in Chapter V. The coefficient was higher for foils in which evidence of crystallinity was found by x-ray diffraction. Eleven of the specimens exhibited coefficients of less than 1.35 x 10^{-4}, and of these, most had coefficients near the rather sharply defined lower limit of 0.90 x 10^{-4}. Since it is likely that the spread of values is caused by varying amounts of crystalline material in the specimens which

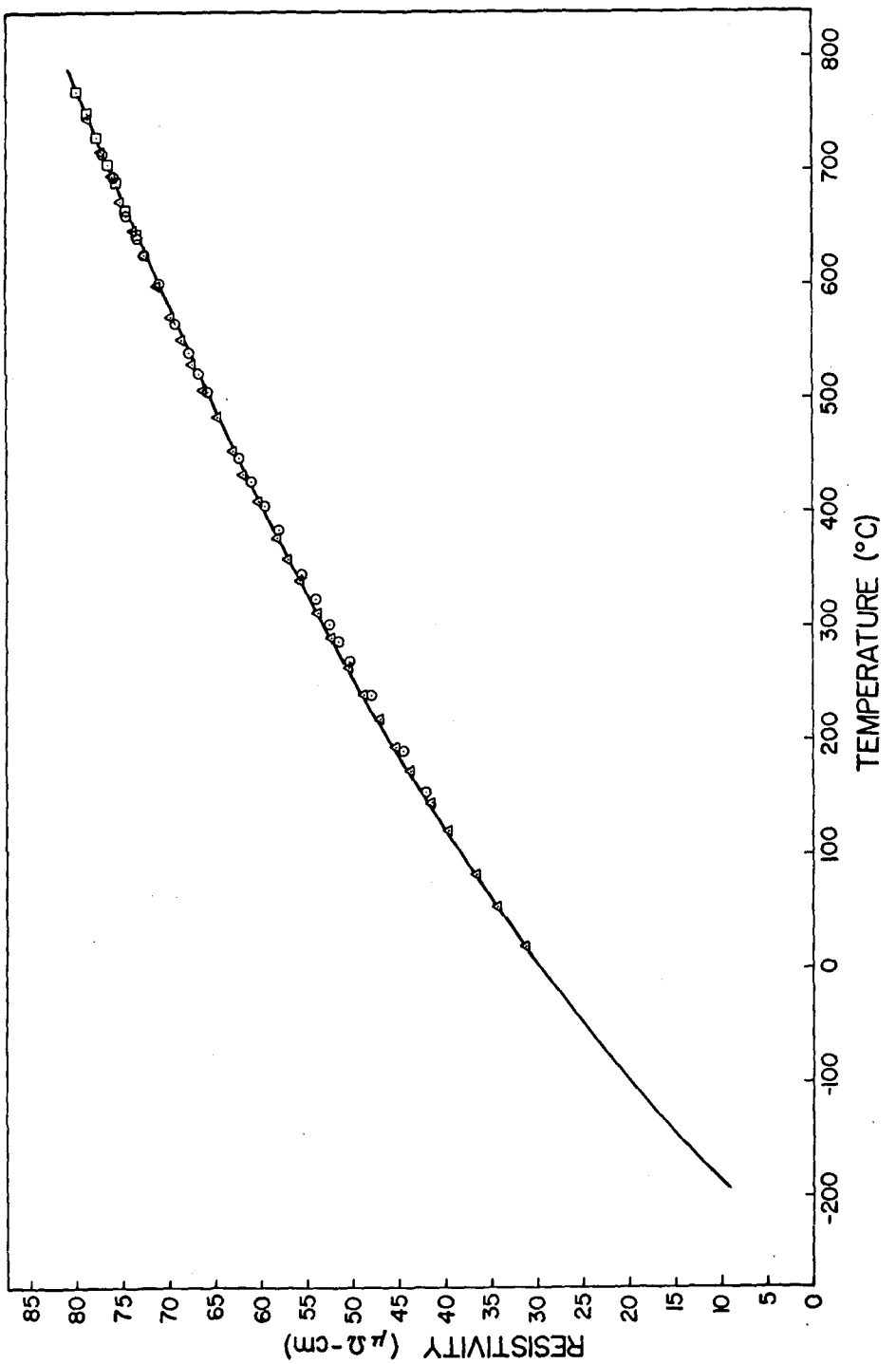

Fig. 6.6. Normalization of the resistance of annealed $Pd_{80}Si_{20}$ foils (data points) to the resistivity of the equilibrium cast specimens (solid line).

would tend to raise the coefficient, the most reliable value to assume for the glass is 0.90×10^{-4}. The temperature coefficient of resistivity $\frac{1}{\rho}\left(\frac{\partial \rho}{\partial T}\right)_P$, calculated by adding the linear coefficient of thermal expansion (see Appendix A) to $\frac{1}{R}\left(\frac{\partial R}{\partial T}\right)_P$ is 1.02×10^{-4}. Thus, since $\rho(20°) = 79.4\ \mu\Omega\text{-cm}$, $\left(\frac{\partial \rho}{\partial T}\right)_P = 0.81 \times 10^{-2}\ \mu\Omega\text{-cm/°C}$ for the $Pd_{80}Si_{20}$ glass, a value which is significantly lower than that measured for the liquid.

B. Discussion. The experimentally determined resistivity data for $Pd_{80}Si_{20}$ (uncorrected for thermal expansion) are summarized in Fig. 6.7. When a correction for the thermal expansion of the amorphous foils is taken into account it is found that the extrapolated resistivity curves of the liquid and glass phases intersect at 430°C ± 30°C. Since the temperature dependence of the resistivity is influenced by the thermal expansion, which is different for the liquid and the glass, it is reasonable to assume that this intersection is the glass point, Tg. It exceeds the temperature range in which the glass is stable because of the rapid cooling rate used. For lower rates of cooling Tg would be expected to be lower.

The fact that the Hall coefficient of the amorphous PdSi foils is practically independent of temperature (1) suggests that the nearly free electron theory of liquid conductors (2, 3, 4) may be applicable to the glass.

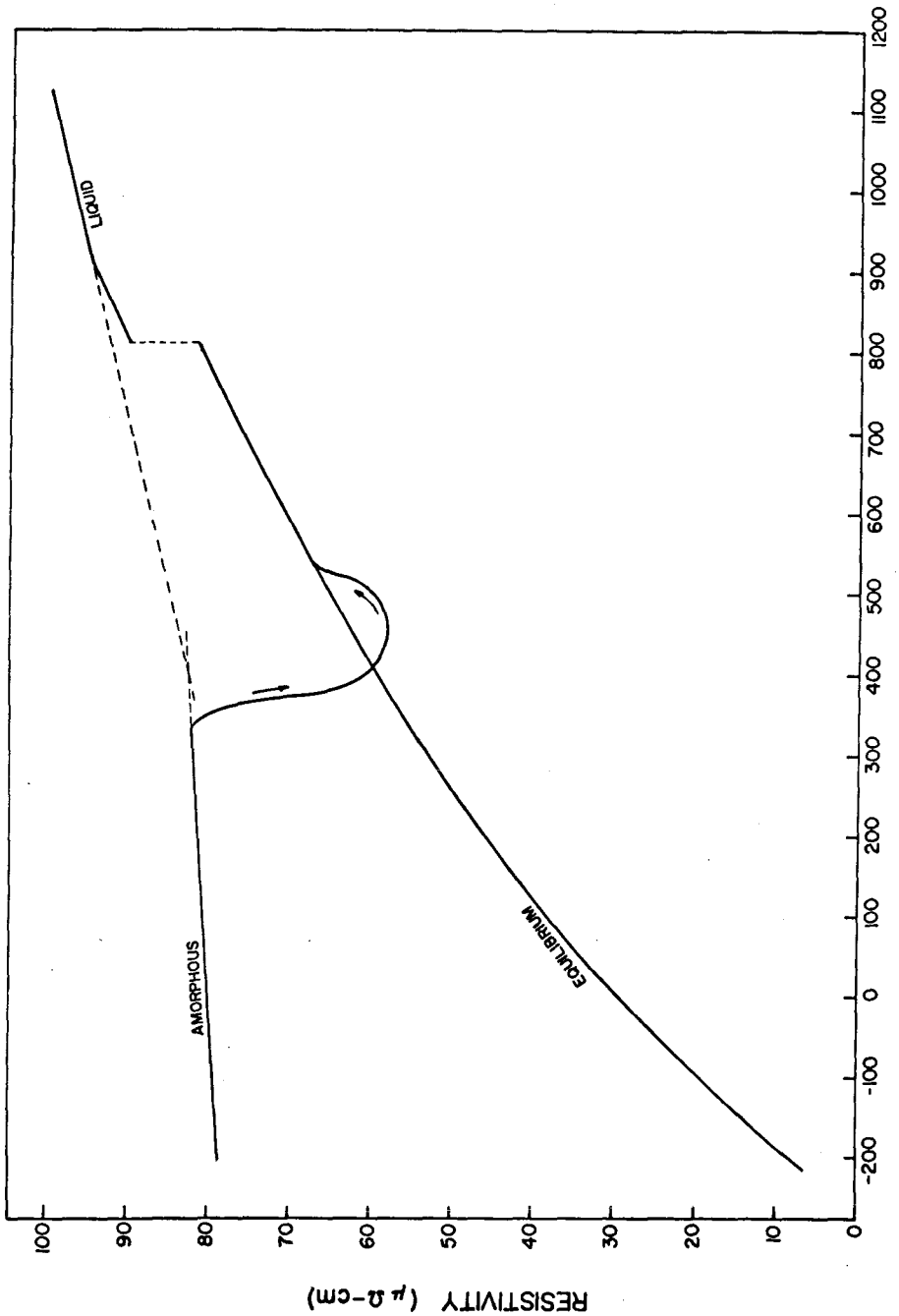

Fig. 6.7. Electrical resistivity of the amorphous, liquid and stable crystalline ("equilibrium") phases of $Pd_{80}Si_{20}$. The section of the graph marked with arrows was obtained from amorphous foils as they crystallized while being heated at a rate of 1.5°C/min.

The conduction electrons are represented in the theory by spherically distributed plane wave states $\vec{k}$, which are occupied only within a Fermi sphere of radius k_F. The electrons are scattered through $\vec{s} = (\vec{k}_{initial} - \vec{k}_{final})$ by the "psuedo potentials" $U_0(r)$ and $U_1(r)$ of the solvent and solute ions respectively. Then for an alloy of concentration c, with random solid solution and in which dilation is not important:

$$\rho = \left(\frac{3\pi N}{\hbar e^2 V v_F}\right)\left\{\int_0^1 [(1-c)a u_0^2 + c a u_1^2]\left(\frac{s}{2k_F}\right)^3 d\left(\frac{s}{2k_F}\right) + \int_0^1 c(1-c)(1-a)(u_1-u_0)^2\left(\frac{s}{2k_F}\right)^3 d\left(\frac{s}{2k_F}\right)\right. \qquad (6.1)$$

where $\frac{N}{V}$ is the ion density, v_F is the Fermi velocity, and u(s) is a Fourier component of U(r). The correlation function a(s), which is a measure of the strength with which an incident beam of electrons is diffracted, is essentially the Fourier transform of the radial density function and can be determined from x-ray diffraction data. The correlation function of $Pd_{80}Si_{20}$, shown in Fig. 6.8, was calculated from:

$$a(s) \approx \frac{I^E(s)}{\langle f^2 \rangle}$$

where $I^E(s)$ is the diffracted x-ray intensity (see Chapter IV) and f is the atomic scattering factor.

It is apparent from Eq. 6.1 that the temperature dependence of ρ is due to thermal expansion and the temperature dependence of a(s). Therefore, if measurements of ρ were

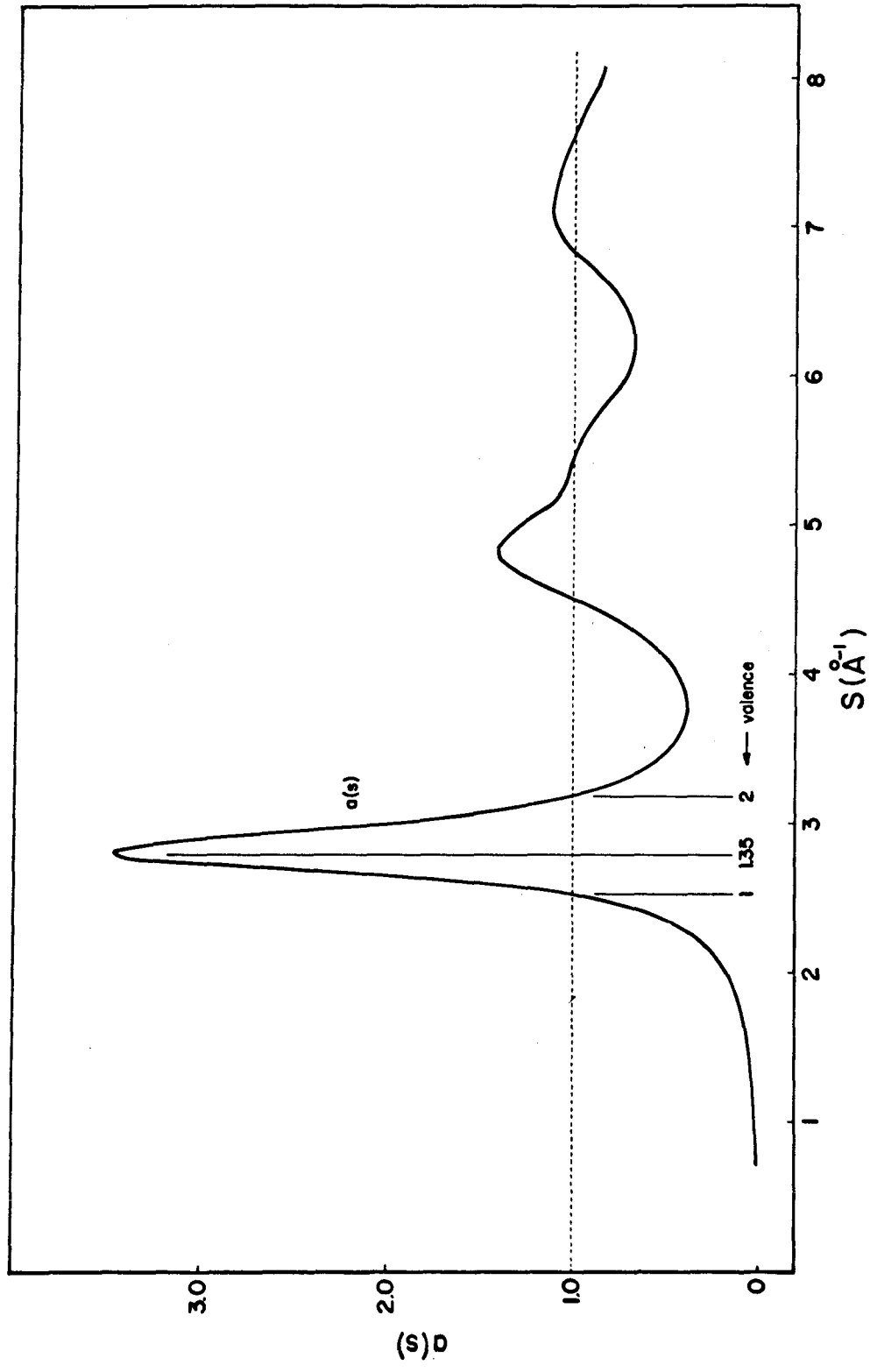

Fig. 6.8. Correlation function of $Pd_{80}Si_{20}$ glass. The vertical lines indicate the magnitude of the Fermi diameter for different numbers of conduction electrons per atom (valence).

made at constant volume rather than constant pressure, only the variation of a(s) would be important in determining $\frac{d\rho}{dT}$. The magnitude of the effect of a(s) upon $\frac{d\rho}{dT}$ should be less at constant volume since this condition should severely limit the possible configurations that the atoms could assume. In the case of the glass this configurational variation should be absent altogether, leaving only the effect of thermal oscillations upon a(s).

The temperature coefficient of ρ at constant volume can be calculated by means of the equation:

$$\frac{1}{\rho}\left(\frac{d\rho}{dT}\right)_V = \frac{1}{\rho}\left(\frac{d\rho}{dT}\right)_P - \frac{3V\alpha}{\rho}\left(\frac{d\rho}{dV}\right)_T \qquad (6.2)$$

where α is the linear coefficient of thermal expansion. The quantity $\frac{V}{\rho}\left(\frac{d\rho}{dV}\right)_T$ was calculated from a semi empirical relationship (2) between it and the thermoelectric power. A preliminary determination (6) that the thermoelectric power of $Pd_{80}Si_{20}$ glass is about $0.0\,\mu V/^{\circ}C$ at $200^{\circ}K$ indicates that $\frac{V}{\rho}\left(\frac{d\rho}{dV}\right)_T \approx 2.6$. By using the measured values of $\frac{1}{\rho}\left(\frac{d\rho}{dT}\right)_P$ and α (see Appendix A), the coefficient of resistivity of $Pd_{80}Si_{20}$ glass at constant volume and at $430^{\circ}C$ was determined to be 0.0×10^{-4}. This compares to 1.0×10^{-4} for the glass at constant pressure, and as expected is much smaller in magnitude. If the main effect of volume change upon the resistivity is not in its effect upon the form of a(s) then it is not unreasonable to expect that $\frac{V}{\rho}\left(\frac{d\rho}{dV}\right)_T$ for the

liquid is nearly the same as that for the glass. On this assumption, and assuming that α for $Pd_{80}Si_{20}$ liquid is the same as that for molten Pd, the temperature coefficient of resistivity at 430°C was estimated as -0.1×10^{-4} at constant volume. This compares to 3.0×10^{-4} at constant pressure. The small magnitude of the coefficient at constant volume, which should be due solely to the effect of changing the form of a(s), supports the validity of the assumption on $\frac{V}{\rho}\left(\frac{\partial \rho}{\partial V}\right)_V$. It is likely that -0.1×10^{-4} is a somewhat low estimate of $\frac{1}{\rho}\left(\frac{\partial \rho}{\partial T}\right)_V$ since α at this low temperature was probably overestimated.

Monovalent liquid metals have a large positive value for $\frac{1}{\rho}\left(\frac{\partial \rho}{\partial T}\right)_V$ because only that part of a(s) to the left of the first peak (see Fig. 6.8) is included in the integrals of Eq. 6.1. This part of a(s) varies linearly with temperature. Divalent metal liquids, however, generally have a negative value for this coefficient due to the contribution of the first peak in a(s), which decreases in intensity as the temperature rises. Since preliminary measurements of the Hall effect indicate an average valence of less than two, it is possible that the above results indicate a transitional situation between the cases of a valence of one and of two.

REFERENCES

1. R. H. Willens, private communication.

2. J. M. Ziman, Phil. Mag., 6, 1013-1034, (1961).

3. C. C. Bradley, T. E. Faber, E. G. Wilson and J. M. Ziman, Phil. Mag., 7, 865-887, (1962).

4. T. E. Faber, and J. M. Ziman, Phil. Mag., 11, 153-173, (1965).

5. J. C. Phillips and L. Kleinman, Phys. Rev., 116, 287, (1959).

6. C. C. Tsuei, private communication.

APPENDIX A

The thermal expansion coefficient of amorphous $Pd_{80}Si_{20}$ was determined from the deflection of a bi-metallic couple specimen made from an amorphous foil and a "reference" foil of Cu, Fe or Pt. A side view of the specimen is shown in Fig. A.1b where a nickel mirror has been spotwelded to one end. Typical dimensions were 1.5 cm. for the foil length l between the copper shims, 0.05cm. for the distance t between the foils, and 1 cm. for the distance c from the mirror to the center point of the foils. The foils were 45μ to 50μ thick and 0.4 cm. wide. A clamping device, which held the specimen at one end, was mounted in an evacuated Pyrex tube (Fig. A.2) and placed in a furnace. As shown in Fig. A.2, the temperature was measured by a thermocouple mounted in a tubular aluminum shield placed around the specimen. Preliminary experiments showed that the temperature obtained in this way was within $0.5^{\circ}C$ of the specimen temperature.

With the aid of a telescope the deflection was read from the image of a scale reflected in the nickel mirror spotwelded to the free end of the specimen. The geometry of this arrangement is shown in Fig. A.1a where r is the radius of curvature of the scale ($r = 50$ cm.), θ is the deflection angle of the specimen and d is the scale reading. The deflection angle θ was always less than 1°.

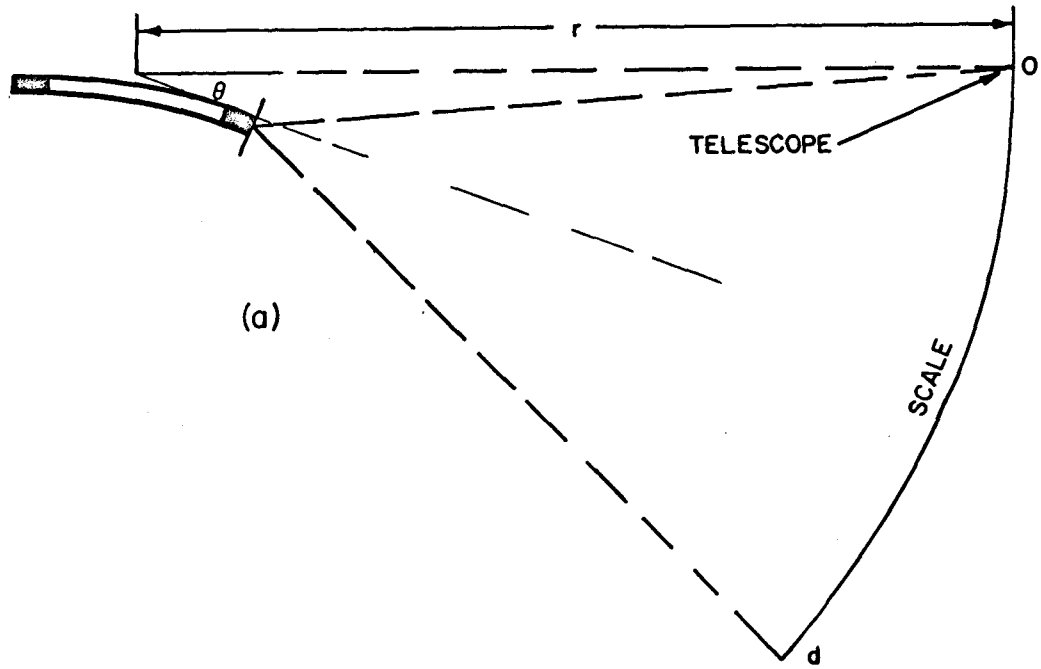

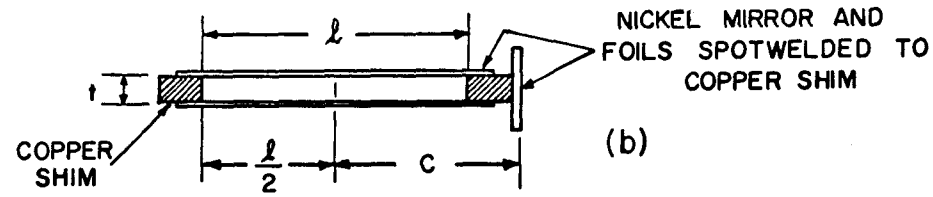

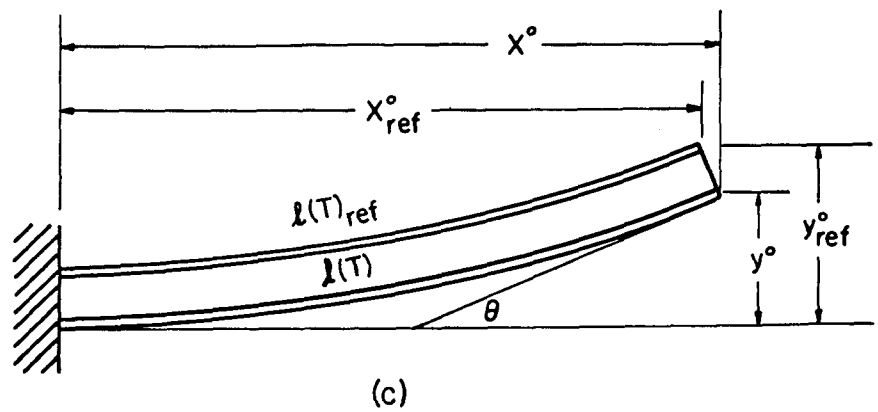

Fig. A.1 (a) Schematic diagram of experimental arrangement used to detect the deflection of a bimetallic couple. (b) Bimetallic couple used in thermal expansion measurements. (c) Deflection of the bimetallic couple when the length of the reference foil $\ell(T)_{ref}$ is less than the length of the $Pd_{80}Si_{20}$ foil $\ell(T)$.

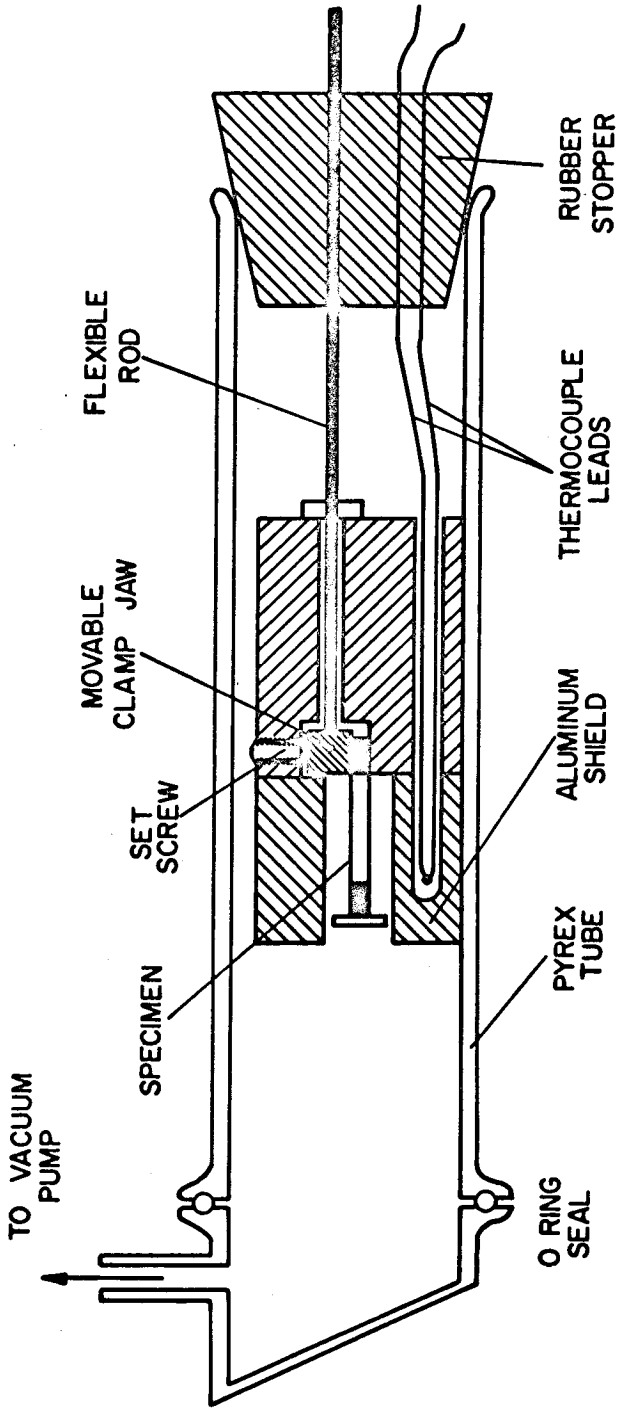

Fig. A.2. Apparatus for mounting thermal expansion specimen. (Diameter of Pyrex tube is exaggerated.)

To eliminate errors due to stress relief in the specimen during the experiment, the specimen was maintained for 24 hours at 200°C before each experiment.

The deflections of specimens made with crystalline $Pd_{80}Si_{20}$ foils (annealed 75 hours at 750°C) were measured in the same manner.

At a temperature T the foils of the reference metal and of $Pd_{80}Si_{20}$ will have lengths $\ell_{ref}(T)$ and $\ell(T)$ respectively. For the case of $\ell(T) > \ell_{ref}(T)$ the specimen will bend as shown in Fig. A.1c. It is convenient to define:

$$\Delta\ell = \ell(T) - \ell$$

$$\Delta\ell_{ref} = \ell_{ref}(T) - \ell$$

where l is the length of both foils at T = 20°C. The dependence of the deflection d upon $\Delta\ell$ and $\Delta\ell_{ref}$ cannot be calculated exactly because the elastic constants of the $Pd_{80}Si_{20}$ foils are not known. However, an approximate calculation indicates that for the deflections used here the bending due to longitudinal and shear stresses in the foils can be neglected in comparison to that due to the bending moment (1). In this case the bi-metallic couple should bend in a circular arc and:

$$\frac{\Delta\ell - \Delta\ell_{ref}}{\ell} \simeq \frac{td}{2\ell(r+c)} \qquad \text{A.1}$$

The quantity $\frac{\Delta\ell - \Delta\ell_{ref}}{\ell}$, calculated from d using Eq. A.1, is plotted in Fig. A.3 for various bi-metallic couples.

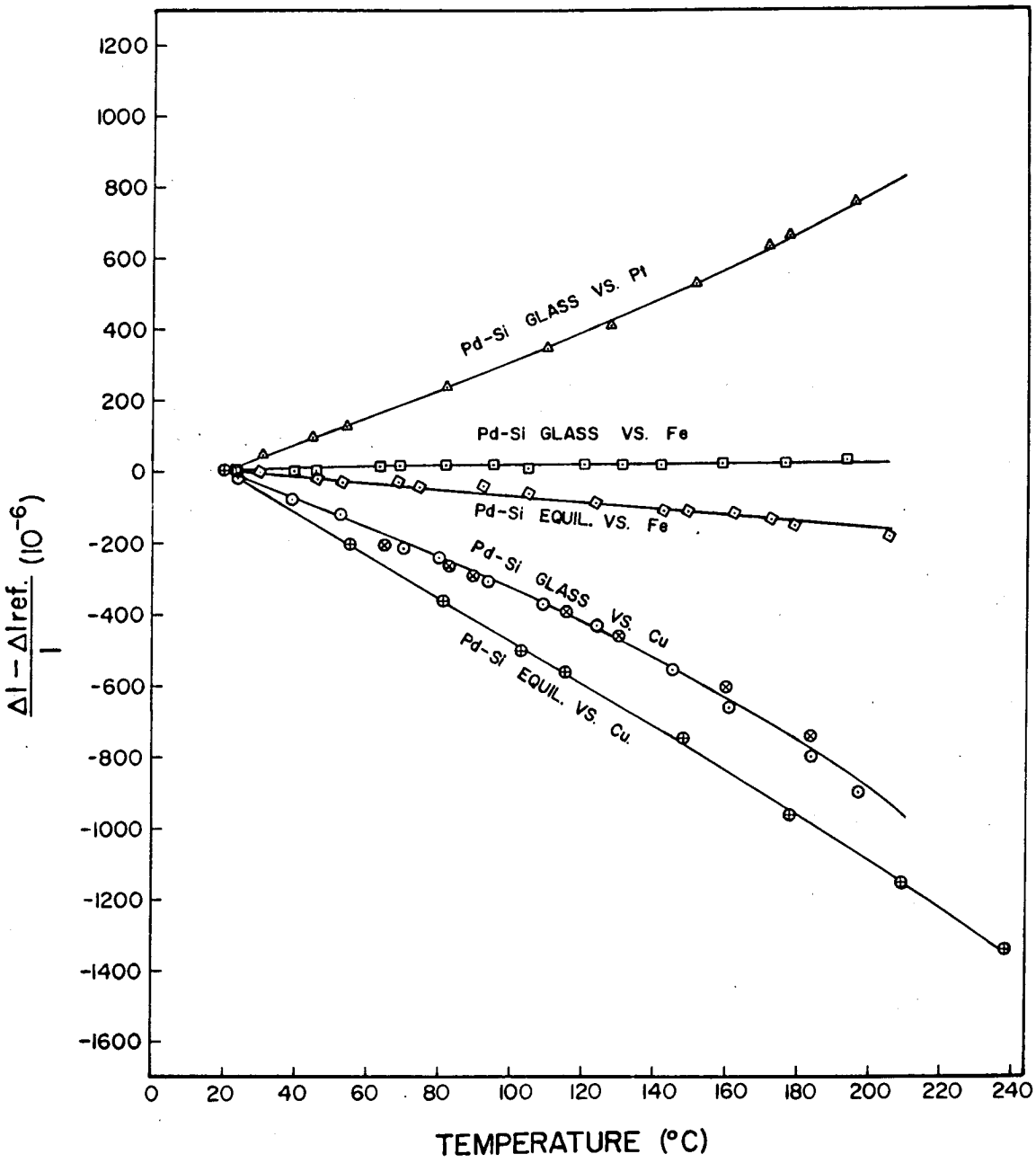

Fig. A.3. Linear thermal expansion (expressed as a function of sample length at 20°C) of $Pd_{80}Si_{20}$ foils relative to that of reference foils of copper, iron or platinum. The $Pd_{80}Si_{20}$ foils had either a glass structure, or an equilibrium crystalline structure attained after an anneal of 75 hours at 750°C.

If longitudinal strain is negligible then:

$$\frac{\Delta \ell_{ref}}{\ell} = \int_{20°C}^{T} \alpha_{ref}\, dT$$

where α_{ref} is the linear thermal expansion coefficient of the reference metal. Thus, the thermal expansion of $Pd_{80}Si_{20}$ is given by:

$$\frac{\Delta \ell}{\ell} = \frac{t\, d}{2\ell\,(r+c)} + \int_{20°C}^{T} \alpha_{ref}\, dT \qquad \text{A.2}$$

The quantity $\frac{\Delta \ell}{\ell}$, calculated for the $Pd_{80}Si_{20}$ foils from Eq. A.2 and published values of α_{ref} for Cu, Fe and Pt (2, 3), is plotted in Fig. A.4. The linear thermal expansion coefficient, calculated from the slope of the curves in Fig. A.4, is given in Table A.1 for crystalline and amorphous $Pd_{80}Si_{20}$ and compared to published values for crystalline and liquid Pd (4, 5).

TABLE A.1

Thermal Expansion Coefficients

of Phases of Pd and $Pd_{80}Si_{20}$

Phase		Temp. Range	α
$Pd_{80}Si_{20}$	glass	20°C - 200°C	12.5×10^{-6}
$Pd_{80}Si_{20}$	crystalline	20°C - 200°C	11.0×10^{-6}
Pd	crystalline	20°C	11.8×10^{-6}
Pd	liquid	1552°C - 1800°C	40×10^{-6}

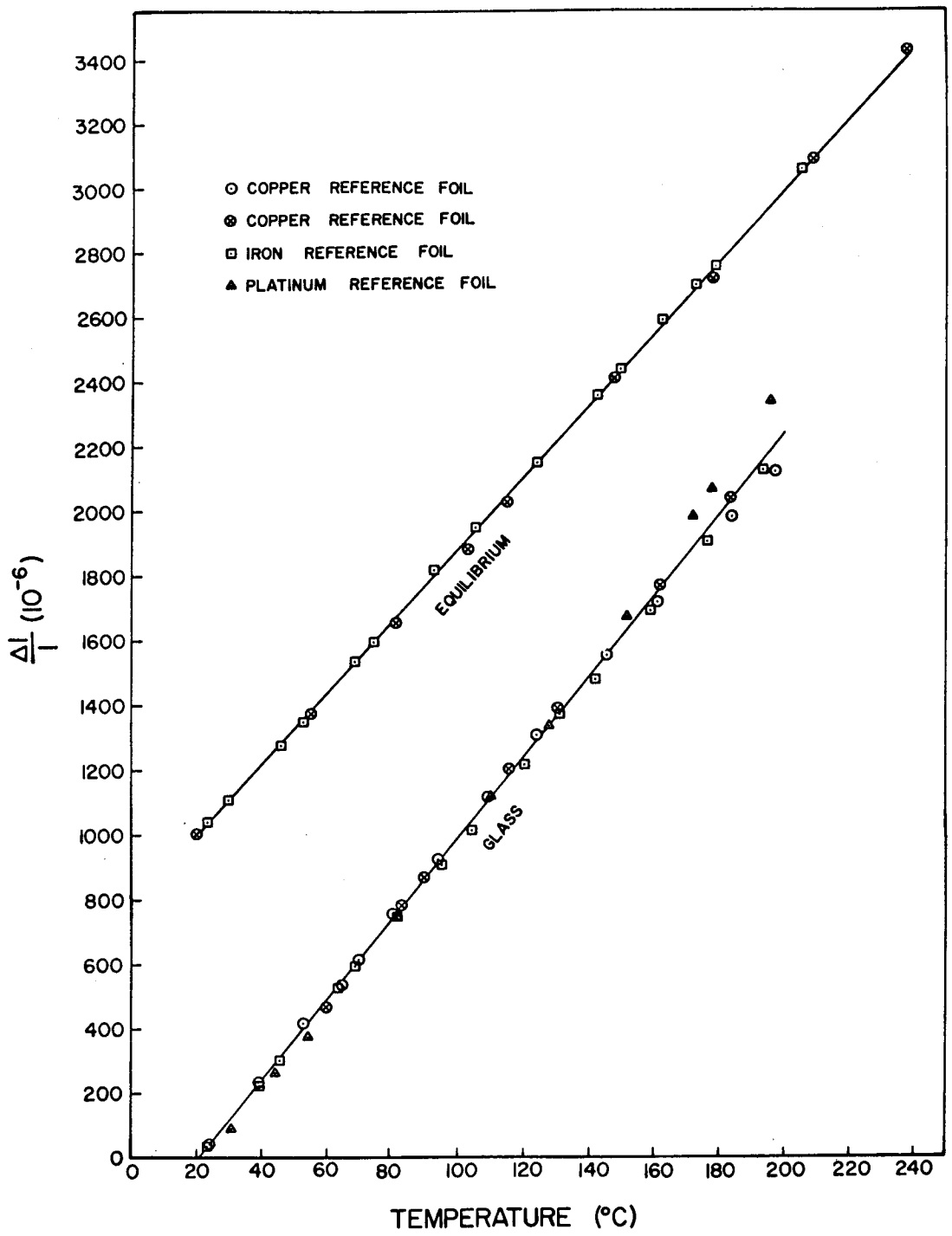

Fig. A.4. Linear thermal expansion (expressed as a function of sample length at 20°C) of glass foils and equilibrium annealed foils of $Pd_{80}Si_{20}$. The curve for the equilibrium annealed foils has been shifted by 10^{-3} along the ordinate.

The good agreement between the sets of $\frac{\Delta \ell}{\ell}$ data plotted in Fig. A.4 supports the validity of the assumptions made in the derivation of Eq. 1. This is true because errors in $\frac{\Delta \ell}{\ell}$ due to noncircular bending should be in different directions for data derived from specimens with Cu and Pt reference foils. In addition the data from specimens with iron reference foils should exhibit negligible errors because of the almost null deflection involved.

REFERENCES

1. D. Pope, private communication.
2. F. Nix and D. MacNair, Phys. Rev., 60, 597, (1941).
3. L. F. Oldfield, Glass Technology, 5, 41-50, (1964).
4. Metals Handbook, 1, 8th ed., 54, (1961).
5. L. D. Lucas, Comptes Rendus, 253, 2526-2528, (1961).

APPENDIX B

A 10 ml. pycnometer, with water as the immersion medium, was used to measure the density of amorphous and crystalline specimens of $Pd_{80}Si_{20}$. The amorphous specimen consisted of 1.5 g. of foils produced by the piston and anvil method and the crystalline specimen was a 7 g. ingot, annealed 150 hours at 750°C. The results of four measurements made upon the amorphous specimen and two measurements on the crystalline specimen are given in Table B.1 where the uncertainty is the spread of values obtained in the independent measurements. The rather small density difference between the two phases (as compared to that between the crystalline and liquid phases of a close packed metal) is easily accounted for by the high thermal contraction of the undercooled liquid.

TABLE B.1

Density of Crystalline and Amorphous $Pd_{80}Si_{20}$

Phase	Density at 20°C
Crystalline	10.50 ± 0.05 g/cc
Amorphous	10.25 ± 0.1 g/cc